Materials Today Bio 29 (2024) 101253

Contents lists available at ScienceDirect

Materials Today Bio

journal homepage: www.journals.elsevier.com/materials-today-bio

Polydopamine-functionalized calcium-deficient hydroxyapatite 3D-printed scaffold with sustained doxorubicin release for synergistic chemo-photothermal therapy of osteosarcoma and accelerated bone regeneration

Lu Wang [a,b,1], Zihan Dai [c,d,1], Jianqiang Bi [a,b,*], Yunzhen Chen [c,**], Ziyu Wang [e], Zhenqian Sun [c,d], Zhongjie Ji [c,d], Hongliang Wang [c,d], Yan Zhang [f], Limei Wang [f], Junjie Mao [a,b], Junxing Yang [a,b]

[a] Key Laboratory for Liquid-Solid Structural Evolution and Processing of Materials (Ministry of Education), Shandong University, Jinan, 250061, PR China
[b] Schools of Materials Science and Engineering, Shandong University, Jinan, 250061, PR China
[c] Department of Orthopedics, Qilu Hospital of Shandong University, #107 Wenhuaxi Road, Jinan, 250061, PR China
[d] Cheeloo College of Medicine, Shandong University, Jinan, 250061, PR China
[e] Department of Orthopaedics, Peking University Third Hospital, Beijing, 100191, PR China
[f] Advanced Medical Research Institute/Translational Medicine Core Facility of Advanced Medical Research Institute, Shandong University, PR China

ARTICLE INFO

Keywords:
Calcium-deficient hydroxyapatite
Polydopamine
Doxorubicin
Antitumor
Photothermal/chemotherapy
Bone regeneration

ABSTRACT

Interior bone-tissue regeneration and rapid tumor recurrence post-resection are critical challenges in osteosarcoma and other bone cancers. Conventional bone tissue engineering scaffolds lack inhibitory effects on bone tumor recurrence. Herein, multifunctional scaffolds (named DOX/PDA@CDHA) were designed through the spontaneous polymerization of Dopamine (PDA) on the surface of Calcium Deficient Hydroxyapatite (CDHA) scaffolds, followed by in situ loading of the chemotherapeutic drug Doxorubicin (DOX). The PDA coating endowed the scaffolds with significant photothermal properties, while the gradual release of DOX provided an effective chemotherapeutic effect. The on-demand release of DOX at tumor sites, triggered by dual stimulation (near-infrared (NIR) light and the acidic pH typical of tumor microenvironments), specifically targets cancer cells, thereby mitigating systemic side effects. These unique characteristics facilitated effective osteosarcoma eradication both in vitro and in vivo. Moreover, the scaffold's composition, which mimics the mineral phase of natural bone and is enhanced by PDA's biocompatibility, promotes critical osteogenic and angiogenic processes. This facilitates not only tumor eradication but also the regeneration of healthy bone tissue. Collectively, this study presents a potent candidate for the regeneration of bone defects induced by osteosarcoma.

1. Introduction

As the most common primary malignant bone tumor, osteosarcoma is highly invasive, characterized by high metastatic potential, poor prognosis, low survival rates, and the significant challenges associated with its early detection [1–3]. Frontline clinicians typically follow a treatment protocol that includes preoperative chemotherapy, surgical resection of the tumor, and postoperative chemotherapy. The therapeutic effect predominantly depends on the surgical elimination of the lesion and the prevention of tumor recurrence or metastasis [4,5]. However, surgical resection often cannot guarantee the complete removal of tumor cells, potentially leaving behind microscopic disease. Additionally, it can result in significant bone defects that require reconstruction. Postoperative chemotherapy can lead to acute toxic reactions, including alopecia, vomiting, myelosuppression, and nephrotoxicity. Furthermore, it may induce the upregulation of high-mobility group (HMG) proteins in surviving osteosarcoma cells, contributing to increased resistance to chemotherapeutic agents [6]. Therefore, there is

* Corresponding author. Schools of Materials Science and Engineering, Shandong University, Jinan, 250061, PR China.
** Corresponding author.
E-mail addresses: bjq1969@sdu.edu.cn (J. Bi), chyz@sdu.edu.cn (Y. Chen).
[1] co-first author.

https://doi.org/10.1016/j.mtbio.2024.101253
Received 18 March 2024; Received in revised form 25 August 2024; Accepted 13 September 2024
Available online 25 September 2024

an urgent need to develop and investigate novel combination therapies and targeted treatments for the comprehensive postoperative management of osteosarcoma, aiming to improve patient outcomes and reduce the likelihood of recurrence and metastasis [7–9].

To fully recover from bone defects caused by osteosarcoma resection, the treatment procedure should not only induce bone tissue regeneration but also address potential residual tumor tissue. This dual challenge necessitates the development of multifunctional scaffolds that offer both anti-tumor activity and support for bone regeneration [10–12]. The term 'calcium phosphate biomaterials' refers to a class of therapeutic and diagnostic materials consisting of diverse phase forms based on the basic elements calcium (Ca), phosphorus (P), and oxygen (O). Among the wide variety of calcium phosphate materials, calcium-deficient hydroxyapatite (CDHA), prepared by self-setting of alpha-tricalcium phosphate (α-TCP) [13], has attracted much attention [14–16]. Compared with the relatively stable conventional calcium phosphate bio-ceramics (hydroxyapatite, HA[17]; beta-tricalcium phosphate, β-TCP [18] and their mixtures in different ratios, biphasic calcium phosphates, BCP [19]), weakly crystalline CDHA possesses the similar physicochemical characteristic as the bone apatite, which is non-stoichiometric and has a variable Ca/P ratio [20]. This incomplete crystal structure makes CDHA more soluble in body fluid, resulting in a higher release rate of bioactive calcium and phosphorus [21]. However, a significant limitation of natural calcium phosphate materials is their inability to counteract the potential proliferation and metastasis of tumor cells. To overcome this limitation, researchers are increasingly exploring ways to functionalize calcium phosphate materials with anti-tumor properties, aiming to inhibit tumor growth and metastasis while preserving their inherent bone regenerative capabilities [22–24].

Among various tumor therapy options, photothermal therapy has emerged as a promising candidate due to its non-invasive nature [25]. Photothermal therapy effectively suppresses tumor cells by locally raising the temperature at the tumor site, leading to different modes of cell death. It also accelerates chemical reactions around the tumor site and has the potential to enhance the efficacy of other therapeutic methods, such as chemodynamic therapy, chemotherapy, and photodynamic therapy [25–27]. Dopamine can spontaneously polymerize due to its slow oxidation in weakly alkaline solutions, granting it photothermal properties that can be customized by adjusting the deposition concentration, laser power and so on, making it an ideal photothermal reagent. Additionally, its superb adhesive properties on surfaces would improve hydrophilicity and roughness thus regulating cell adhesion, migration and differentiation [27–29]. However, the application of dopamine on CDHA scaffold remains underexplored. Furthermore, postoperative chemotherapy remains prevalent in tumor treatment, and doxorubicin (DOX) has been widely used as a fundamental drug for treating osteosarcoma for more than forty years. Although DOX has significant clinical benefits in treating osteosarcoma, it is associated with a notable risk of heart disease, especially with systemic administration for 6–8 months [30,31]. This is because less than 10 % of the drug is delivered to the tumor site, even with the most advanced systemic delivery systems. The construction of an in-situ delivery platform for DOX plays an important role in preventing premature release, avoiding unwanted systemic side effects, and increasing the effective concentration at the tumor site [32–34].

In this paper, we develop a bifunctional therapeutic platform for bone regeneration and anti-tumor treatment based on three-dimensional calcium-deficient hydroxyapatite scaffolds coated with polydopamine and loaded with doxorubicin. T The three-dimensional calcium-deficient hydroxyapatite scaffold, featuring a gradient pore structure, is fabricated using extrusion-based 3D printing, followed by self-setting in a mild body fluid environment. The polydopamine coating is formed through the self-polymerization of dopamine under weak alkaline conditions, followed by the in-situ adsorption of doxorubicin. Polydopamine, known for its excellent photothermal conversion efficiency in the NIR-I region, endows the scaffold with photothermal therapy capability. The elevated temperature achieved through photothermal therapy triggers the controlled slow release of the chemotherapeutic drug doxorubicin. The three-dimensional porous scaffold guides the formation of the nascent bone matrix and the three-dimensional growth of bone tissue. Therefore, the scaffold can promote bone repair while realizing the photothermal/chemotherapeutic synergistic treatment of residual cancer cells in bone and surrounding tissues. To inhibit bone tumor recurrence post-resection, the scaffold combats tumor cells via two mechanisms: its excellent NIR-I photothermal properties for photothermal ablation of tumors and the sustained release of doxorubicin, which induces tumor cell apoptosis. For the repair of bone defects after bone tumor resection, the scaffold promotes bone repair through two osteogenic/angiogenic pathways. First, the release of calcium and phosphorus ions from the three-dimensional porous, weakly crystalline calcium-deficient hydroxyapatite contributes to new bone formation. Second, the polydopamine coating enhances osteogenic and angiogenic properties. Therefore, the proposed DOX/PDA@CDHA scaffold has good prospects for application in bone regeneration and inhibition of tumor recurrence after bone tumor resection.

2. Materials and methods

2.1. Preparation of calcium deficient hydroxyapatite porous three-dimensional scaffolds

All the chemicals and instruments used in this paper were listed as Table S1. Based on previous studies [35,36], we utilized a slightly modified co-precipitation method for the preparation of alpha-TCP. Before use for 3D extrusion printing, the powder was wet-milled in alcohol to achieve homogenization. Subsequently, according to the formulation of 7 g alpha-TCP/0.6 g sodium alginate/15 g F-127 (20 wt %) aqueous solution, the printing slurry was obtained by mixing and defoaming using a centrifugal homogenizer. 3D printing was carried out according to the pre-designed program. The printed scaffolds were dried at room temperature overnight, held at 600 °C for 3 h to remove organic matter, and subsequently soaked in PBS solution (pH = 7.4) at 37 °C for 4 days before being dried and set aside. Theses scaffolds were named as CDHA scaffold.

2.2. Preparation of polydopamine coating and in-situ loading of doxorubicin

To prepare CDHA scaffolds with a surface-deposited polydopamine coating, dopamine hydrochloride was weighed and dissolved in Tris-HCl solution at pH 8.5 to prepare graded concentrations of dopamine solution (2 mg/ml, 4 mg/ml, 6 mg/ml). The CDHA scaffolds were then immersed in the dopamine-Tris-HCl solution for 24 h, followed by drying in an oven at 40 °C for 24 h. The polydopamine-coated CDHA scaffolds, named PDA@CDHA scaffold, were obtained. To evaluate the loading capacity of the composite scaffolds on Doxorubicin, the PDA@CDHA scaffolds were immersed in a deionized water solution of Doxorubicin. After shock adsorption for 24 h, the scaffolds were cleaned and then dried in an oven at 40 °C for 24 h. The polydopamine-coated CDHA scaffolds adsorbed on Doxorubicin were obtained and named DOX/PDA@CDHA scaffold.

2.3. Characterization of three-dimensional scaffolds

The rheological behavior of the slurries was measured by modular compact rheometer MCR302 (Anton Paar, GmbH, Austria). The surface topographic structure and 3D morphology of the 3D scaffolds were characterized by scanning electron microscopy (JSM7800F, Rigaku, Japan), energy spectrum analyzer (NordlysMax3, Oxford Instruments, UK), and white-light interferometric confocal microscopy (LSM800, Zeiss, Germany). The water contact angle of the samples was characterized by a contact angle measuring instrument (DSA100S, Kruss,

German). The physical phase composition and surface functional group distribution were characterized by X-ray diffraction instrument (DMAX-2500PC, Rigaku, Japan) and ATR-FTIR spectrometer (Thermo-Nicolet Nexus 670, Renishaw, UK) The absorbance at 808 nm of the scaffolds was tested for subsequent testing of the photothermal conversion efficiency of the scaffolds using a UV–visible near-infrared spectrophotometer (UV-3600i Plus Shimadzu, Japan). The ζ-potential of the crushed powder of the 3D scaffolds was measured using a Zetasizer range (Zetasizer, Malvern, China).

2.4. Characterization of scaffold photothermal performance

To evaluate the photothermal ability of the PDA@CDHA scaffolds, the scaffolds were placed into a 48-well plate, followed by the addition of 400 μl of phosphate buffer (pH 7.4). The scaffolds were subsequently irradiated with a near-infrared laser of 808 nm for 80 s. The temperature of the scaffolds was monitored by a thermal camera and the effects of different laser powers on the photothermal performance of the scaffolds were revealed. In order to verify the stability of the photothermal performance of the scaffolds, the scaffolds were exposed to the 808 nm laser (1 W/cm^2) and the laser was turned off after warming up to the equilibrium temperature. Then the laser irradiation was restarted after completely cooling down to room temperature. The operation was repeated three times while the temperature curves of the scaffolds were recorded. Based on the cooling curve of the scaffold, the photothermal conversion efficiency of the scaffold was calculated.

2.5. Characterization of loading and release performance of doxorubicin

To evaluate the loading ability of PDA@CDHA scaffold for DOX, DOX was dispersed in deionized water and configured into a solution for spare (0.4 mg/ml). Considering the different sizes of the printed scaffolds, we adopted mass proportioning to record the loading performance. 40 ml of the above solution was added to a large centrifuge tube containing 0.3 g of PDA@CDHA scaffolds and was shaken slowly for 12 h. Then, the scaffolds were washed with deionized water and dried to obtain DOX/PDA@CDHA scaffold while all the solution was collected. Absorbance at 450 nm before and after the adsorption were measured using a UV spectrophotometer to calculate the encapsulation rate (E. E. %) of DOX on the scaffolds. A similar method was used to investigate the release properties by characterizing the DOX concentration around the scaffolds. Specifically, in order to mimic and guide the in vitro antitumor experiments as much as possible, we took the same scaffold/incubation solution ratio and submerged the DOX/PDA@CDHA scaffold into PBS in order to investigate DOX release behavior triggered by the NIR light and the acid-base conditions. 0.5 ml of the solution was removed and an equal amount of fresh PBS was added at different time points. An 808 nm laser was used so that the temperature of the scaffolds was maintained at 48 °C for about 15 min to explore the effect of NIR light on DOX retardation. PBS solutions with different pH values (5.0, 6.0, 7.4) were used to investigate the effect of the medium on the release of DOX.

2.6. In vitro anticancer effects of composite scaffolds

Osteosarcoma cells (MG63 and HOS, Zhongqiao Xinzhou Biotechnology Co., Ltd, Shanghai, China) were cultured in DMEM medium containing 10 % fetal bovine serum and 1 % penicillin/streptomycin in a humidified incubator (5 % CO_2 at 37 °C).

Cell Proliferation and Toxicity Assay was performed after as high as 3 days of culturing with different samples. The cells were seeded into 12-well plates (2.0 × 10ˆ5 cells per well) and allowed to adhere and grow until confluence reached 80 %. Samples were divided into different groups and co-cultured with sterilized scaffolds. For groups requiring photothermal treatment, a laser with a wavelength of 808 nm and a power density of 1.0 W/cmˆ2 was used for irradiation for 5 min daily. After a maximum of three days of treatment, cell proliferation was assessed using the CCK-8 assay (C0038, Beyotime China) at 450 nm. The Live/Dead staining assay were carried out to assist above-mentioned experiment. After treatments, cells were stained with a mixture of propidium iodide (PI) and calcein (AM) (C2015M, Beyotime China), incubated at 37 °C in the dark for 30 min, and observed under a fluorescence microscope (Zeiss Germany).

Apoptosis assay was performed after 12 h of culturing with different samples. The apoptosis and necrosis of HOS and MG63 cells were detected using the Annexin V-FITC/PI apoptosis detection kit (A211-01/02, Vazyme China). Cells with a confluence of about 80 % were collected using trypsin without EDTA, resuspended, and washed with PBS. Then, 5 μL Annexin V-FITC and 5 μL PI were used for staining at room temperature in the dark for 20 min. The stained cells were analyzed using flow cytometry (Beckman USA).

To evaluate apoptosis-related gene expression, cells (MG63 and HOS) cultured with composite scaffolds were harvested and TRIZOL (YS143200, Solarbio China) was used to extract RNA from cells. cDNA was synthesized from the extracted mRNA using the HiScript III RT SuperMix for qPCR kit(R323, Vazyme China). ChamQ Universal SYBR (Q711-02/03,Vazyme China) was used for real-time quantitative reverse transcription polymerase chain reaction (qRT-PCR). Qualitative analysis was performed using the Light Cycler 480 system (Roche Applied Science Germany). The primer sequences are listed in Table S2.

To evaluate apoptosis-related protein expression, Prior to protein extraction, cells (MG63 and HOS) cultured with composite scaffolds were washed twice with phosphate buffered saline (PBS) before the protein extraction. Total proteins of the samples were extracted on ice using a protein extraction kit (BestBio, China) according to the instructions. Protein concentration was determined using the BCA Protein Detection Kit (Beyotime, China). Proteins were mixed with 5 × SDS-PAGE Sampling Buffer (Beyotime, China) and boiled for 10 min. Proteins were separated using the PAGE Gel Rapid Preparation Kit (Epizyme, USA) and transferred to polyvinylidene fluoride (PVDF) membranes (Millipore Sigma, USA). All antibodies were diluted according to the manufacturer's instructions.

Caspase 3 and Caspase 8 activity assay was furthermore conducted to confirm the protein expression level. Cells were seeded into 6-well plates (5.0 × 10ˆ5 cells per well) and allowed to grow until confluence reached 80 %. After two days of treatment according to the grouping scheme, caspase 3 and caspase 8 activity was measured using the Caspase 3 (C1116, Beyotime China) and caspase 8 activity assay kit (C1151, Beyotime China) at 405 nm.

For invasion assay, transwell chambers (with polycarbonate membrane) were placed in 24-well plates, with 100 μl of diluted Matrigel matrix (M8370, Solarbio China) added to each chamber. After two days, cells were digested and resuspended with trypsin, and 1.0 × 10ˆ5 tumor cells were suspended in 200 μl of low serum culture medium (1 % serum content) in the upper chamber, with 600 μl of complete culture medium added to the lower chamber. After 24 h, the transwell chambers were removed, fixed with 4 % paraformaldehyde, stained with crystal violet for 30 min, and washed with PBS to remove unbound dye. Cell invasion was quantified using an inverted microscope by comparing the number of cells that had crossed under different conditions.

For migration assay, this paper used two approaches to verify migration capacity. In the case of Transwell Assay, Transwell chambers were placed in 24-well plates and treated cells were digested and resuspended as described above. After two days of culture, 1.0 × 10ˆ5 tumor cells were suspended in 200 μl of low serum culture medium in the upper chamber, with 600 μl of complete culture medium in the lower chamber. After 12 h, the Transwell chambers were removed, fixed, stained, and washed as described above. Cell migration was quantified by comparing the number of cells that had crossed under different conditions. While in the case of Scratch Assay, cells were seeded into 6-well plates (5.0 × 10ˆ5 cells per well) and allowed to adhere and grow until confluence. A straight line was drawn using a 20-μL pipette tip to create a "scratch" in the cell monolayer. After washing with PBS to

remove cell debris, low serum culture medium (1 % serum content) was added to reduce cell proliferation. Images of the scratch area were taken using an inverted microscope at 0, 6, 12, and 24 h to record the cell migration process. The migration speed was assessed by comparing the reduction in the scratch area over time.

2.7. In vivo anticancer effects of composite scaffolds

4-week-old BALB/c mice were purchased from Beijing Vital River Laboratory Animal Technology Co., Ltd. and housed at the Experimental Animal Center of Qilu Hospital, Shandong University, with a temperature of 23–25 °C and a 12-h light/dark cycle, and provided with sufficient water and food. The animal experiments were approved by the Animal Ethics Committee of Qilu Hospital, Shandong University (Approval No.: Dwll-2023-135). All animal experiments were conducted with the aim of minimizing animal suffering.

Each mouse was injected subcutaneously with 5 × 10^6 HOS cells to establish a tumor-bearing mouse model. When the tumor volume reached approximately 100 mm^3, the tumor-bearing nude mice were randomly divided into 5 groups, with 5 mice per group (N = 5, n = 5 per group). After anesthesia with 3 % pentobarbital sodium, the mice were treated as follows: blank control (sham surgery group), implantation of PDA@CDHA scaffold, implantation of PDA@CDHA scaffold with daily laser irradiation, implantation of DOX/PDA@CDHA scaffold, and implantation of DOX/PDA@CDHA scaffold with daily laser irradiation. The laser power density for photothermal therapy was 1W/cm^2, and the duration of treatment was 5 min. Real-time temperature monitoring of the scaffold was performed using an infrared thermal imaging system. Mice were weighed and tumor volumes were measured every two days. On day 14, mice were sacrificed, and tumors from each group were harvested for H&E staining, TUNEL staining, and immunohistochemistry (Ki-67). Additionally, major organs (heart, liver, spleen, lung, kidney) were harvested for H&E staining.

2.8. In vitro osteogenic and angiogenesis effect of composite scaffolds

Mouse Bone Marrow Mesenchymal Stem Cells (BMSCs), isolated from the tibia and femur of 8-week-old mice using the bone marrow flushing method, were cultured in αMEM medium containing 10 % fetal bovine serum and 1 % penicillin/streptomycin in a humidified incubator (5 % CO_2 at 37 °C). Human Umbilical Vein Endothelial Cells (HUVECs, Zhongqiao Xinzhou Biotechnology Co., Ltd, Shanghai) were cultured in ECM medium containing 5 % fetal bovine serum, 1 % endothelial cell growth factor and 1 % penicillin/streptomycin in a humidified incubator (5 % CO_2 at 37 °C).

In terms of the morphology and adhesion of BMSCs and HUVECs, Cell nuclei and cytoskeleton of cells were stained with DAPI (blue fluorescence) and rhodamine phalloidin (green fluorescence) solution, respectively. Then the samples were observed by CLSM. Meanwhile, scaffolds were fixed with 4 % paraformaldehyde and then dehydrated with gradient concentrations of ethanol (30, 40, 50, 60,70, 80, 90, 100 v/v%). Subsequently, the samples were observed by SEM. The Live/Dead staining, cell proliferation, qRT-PCR, Western plot and apoptosis assay followed the similar procedure as the MG63/HOS cells.

For ALP activity, BMSC were seeded into 12-well plates (2.0 × 10^5 cells per well) and allowed to adhere and grow until confluence. According to the grouping scheme, cells were gently placed into sterilized scaffolds CDHA and PDA@CDHA, and the culture medium was changed every two days for a total of 7 days. ALP activity was measured using an alkaline phosphatase detection kit(P0321M, Beyotime China) at 405 nm, following the manufacturer's instructions. For ALP Staining, BMSCs were seeded into 12-well plates and allowed to adhere and grow until confluence. Following the grouping scheme, cells were gently placed into sterilized scaffolds CDHA and PDA@CDHA, and the culture medium was changed every two days for a total of 7 days. After washing and fixing with 4 % paraformaldehyde for 30 min, BCIP/NBT alkaline phosphatase color development kit(C3206, Beyotime China) was used for incubation at room temperature in the dark for 12 h. The color development reaction was stopped, and cell staining was observed under a microscope (Zeiss Germany).

For ARS Staining, BMSCs were seeded into 12-well plates and allowed to adhere and grow until confluence. Following the grouping scheme, cells were gently placed into sterilized scaffolds CDHA and CDHA + PDA, and the culture medium was changed every two days for a total of 21 days. After washing and fixing with 4 % paraformaldehyde for 30 min, Alizarin red staining kit(G1452, Solarbio China) was used for incubation at room temperature in the dark for 12 h. The color development reaction was stopped, and the number of mineralized nodules was observed under a microscope (Zeiss Germany).

For migration Assay, the similar scratch assay was proceeded except the scratch area was imaged at 0 and 12 h. For Angiogenesis Assay, HUVEC were co-cultured with scaffolds for two days, digested, and resuspended with trypsin, and 50 μl of Matrigel was added to each well of a 96-well plate. After incubation in a CO_2 incubator for 2 h to allow Matrigel to solidify, 5 × 10^4 cells were seeded per well. After 4 h, the formation of vascular-like structures on the Matrigel was observed and recorded using an inverted microscope. Image J software was used to analyze the number of junction points and segments length of tubular networking.

2.9. In vivo osteogenic and angiogenesis effect of composite scaffolds

Eight-week-old male SD rats were purchased from Beijing Vital River Laboratory Animal Technology Co., Ltd. The rats were placed in the Laboratory Animal Center of Qilu Hospital, Shandong University, and fed in an air-conditioned room at 23–25 °C, with a light-dark cycle time of 12 h, and provided with sufficient water and food.

The cranial defect model was established. The rats were anesthetized with 3 % sodium pentobarbital (intraperitoneal injection) and the surgery was performed along the sagittal suture by drilling a hole with a diameter of 5 mm and a depth of 0.5 mm. The rats were randomly divided (number of groups N = 3, n = 5 rats in each group) and treated as follows: blank control (sham-operated group), implantation of Sample CDHA scaffolds and implantation of Sample PDA@CDHA. The scaffolds (3 mm in diameter and 0.5 mm in height) were placed into the side along the edges of the defect. The periosteum was sutured to the defect tissues and the skin one after the other. The rats were euthanized 8 weeks after scaffold implantation and the skulls were harvested and analyzed by Micro-CT imaging.

A Micro-CT imaging system (PerkinElmer; Quantum GX2) was used to scan the skull tissue. The parameters were adjusted to 90 kV, 88 μA for 10 min and 36 μm pixel size resolution. Images were reconstructed using Skyscan NRecon software, and sample parameters were analyzed using CTVox software.

2.10. Statistical analysis

The results are expressed as mean ± standard deviation. All experiments were repeated from three to six times. Statistical differences were determined using one-way analysis of variance statistical method (ANOVA) via SPSS 26.0 software. Levene's test was used for homogeneity of variance test. In case of non-significance, the Bonferroni test was applied for post hoc multiple comparisons. In case of significance, Tamhane's post hoc test was used. The annotation of significance level for post hoc multiple comparison was based on the guideline of emphasizing the superiority of bifunctional scaffold. A p value was 0.05 was considered as a significance level, and the data was indicated with (*) for $p < 0.05$, (**) for $p < 0.0$ and (***) for $p < 0.001$, respectively.

3. Results and analysis

Postoperative osteosarcoma sites require simultaneous bone

regeneration and inhibition of tumor recurrence. Traditional systemic injection methods result in low utilization of postoperative chemotherapeutic drugs, whose adverse effects further retard bone regeneration. Although traditional 3D-printed calcium phosphate scaffolds offer a favorable environment for bone repair, they are not sufficiently effective in eradicating potential bone tumor cells. Inspired by polydopamine's excellent adhesion and customizable photothermal properties, this study leverages three-dimensional extrusion printing technology and the self-assembly of polydopamine under alkaline conditions, complemented by the physical adsorption of chemotherapeutic drugs. This approach results in the fabrication of 3D porous calcium-deficient hydroxyapatite scaffolds coated with dopamine and containing Doxorubicin (see Scheme 1). This method achieves effective tumor growth inhibition both in vitro and in vivo through photothermal/chemotherapeutic synergistic treatment. Additionally, the dopamine coating enhances osteogenic and angiogenic properties in vitro and in vivo.

3.1. Preparation and characterization of DOX/PDA@CDHA

The design and preparation of slurry with suitable rheology is the key to materializing 3D extrusion printing [37]. We initially investigated the rheological behavior of slurries with varying solid contents of alpha-tricalcium phosphate (α-TCP) as shown in Fig. 1. The shear rate-viscosity results in Fig. 1(a) demonstrate that increasing the alpha phase enhances the viscosity of the ink without altering the shear-thinning characteristics of the initial hydrogel. This modification facilitates ink flow at low viscosity under high shear rates (within the 3D printing cylinder) and gradual consolidation at high viscosity under low shear rates (upon extrusion from the nozzle) [38]. As the shear rate increases, the shear stress also increases smoothly (Fig. 1(b)). The rapid decrease in stress at high shear rates, particularly evident at a 35 % solid phase mass fraction, corresponds to a significant reduction in viscosity (Fig. 1(a)). This indicates the slurry's inability to withstand high-speed shear without structural damage. The effects of different solid phase contents on the storage/loss modulus and yield strength of the slurries were investigated as shown in Fig. 1(c) and (d). Taking the mass fraction of 33 % as the example, all the tested inks follow the similar trend. Under low deformation, a linear viscoelastic behavior hydrogel is categorized (at this time, the storage modulus is larger than the loss modulus, and the sample presents a stable solid-like state). With the increase of deformation, the storage modulus (G′) and the loss modulus (G″) are both sharply decreased and intersected, which is attributed to the change of the powder agglomeration structure within the inks, showing the transition from an elastic deformation behavior to plastic deformation behavior. The latter favors the laminar flow of the ink through the extrusion nozzle [39]. The yield point, defined by the intersection of the storage modulus (G′) and the loss modulus (G″), is illustrated in Fig. 1(d), showcasing the flow properties of various inks at this critical juncture. The results show that the incorporation of alpha-TCP in the gel greatly improves the storage/loss modulus and yield strength of the ink but reduces the strain value at the yield point. The effects of the above parameters on printing performance could be interdependent. But generally speaking, the high yield stress with rapidly decreasing viscosity produces sufficient extrudability and higher printing accuracy, whereas storage modulus beyond the appropriate level leads to extrusion discontinuity, furthermore exorbitant loss modulus leads to diffusion

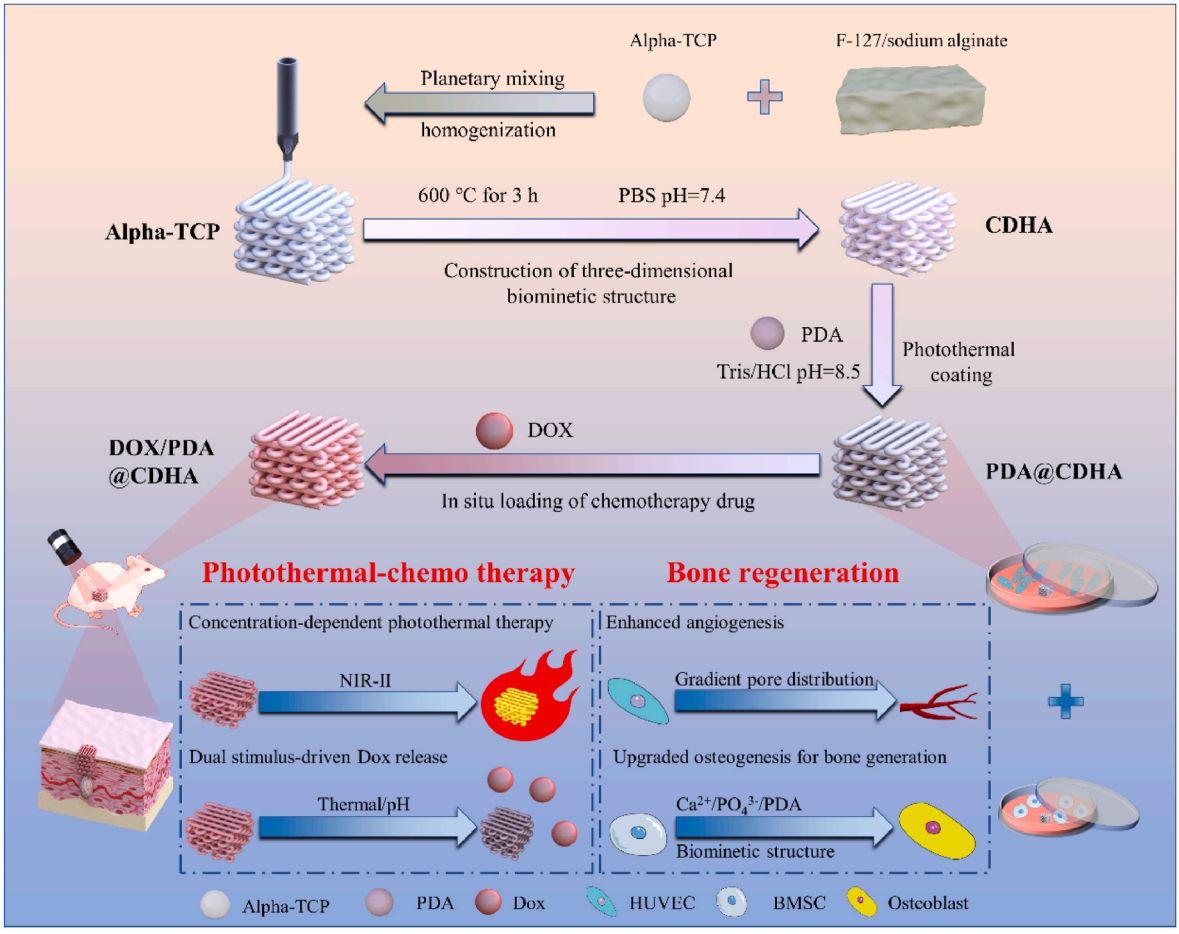

Scheme 1. Schematic illustration of PDA-coated 3D printed CDHA scaffolds with NIR-triggered drug release of DOX for synergistic photothermal/chemotherapy of osteosarcoma.

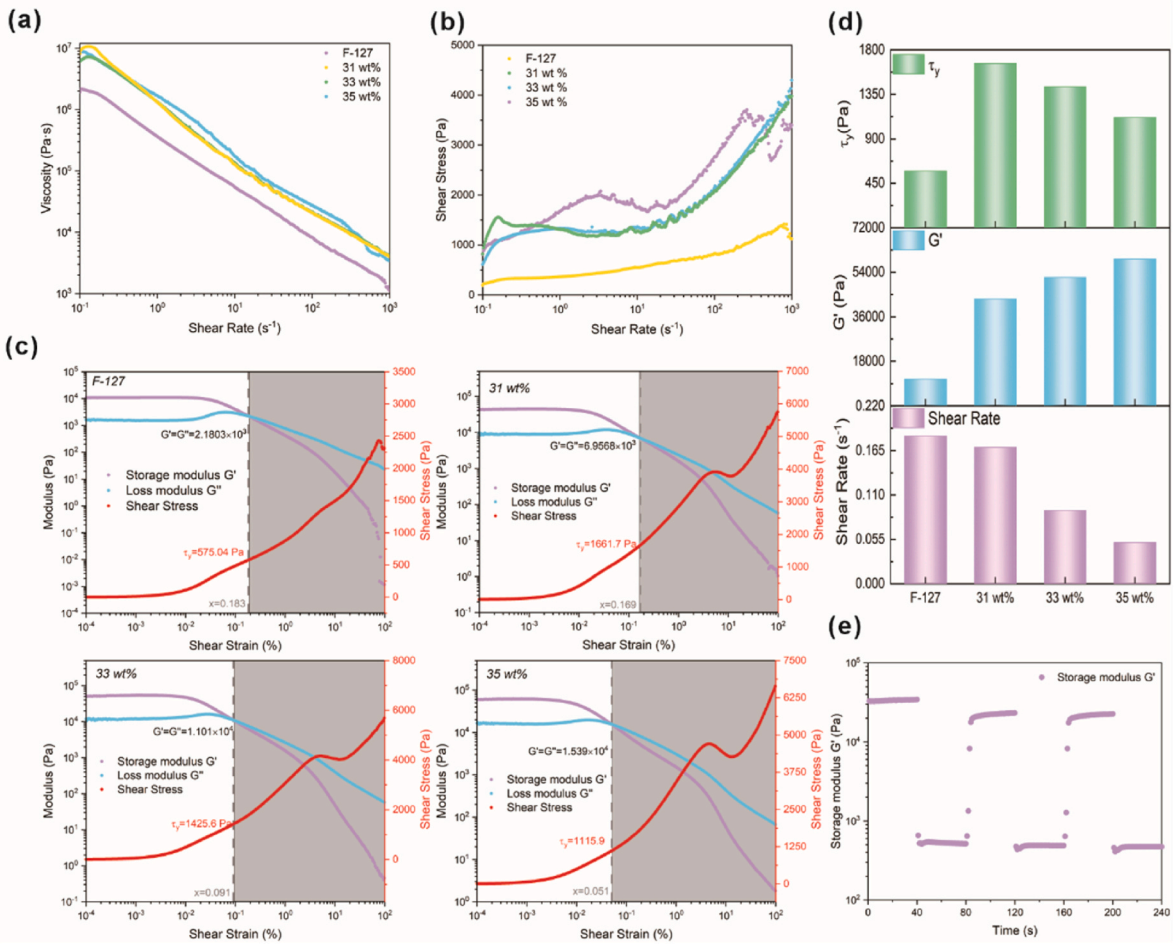

Fig. 1. Rheological properties of the α-TCP slurries. Viscosity vs Shear rate (a), Shear stress vs Shear rate (b), Dynamic moduli and Shear stress vs Shear strain (c) of slurries with different solid contents (0, 31 %, 33 %, 35 %). Flow properties of different slurries at the yield point (d). Modulus stability under oscillatory conditions of slurry under solid content of 33 % (e).

during line deposition, which reduces the extrudability and the accuracy of the printed pattern [40]. Due to challenges in achieving continuous and uniform printing lines with a 35 % mass fraction, we selected the 33 % mass fraction ink for further research. Given the characteristic of three-dimensional extrusion printing, where the ink is subjected to fluctuating pressure accumulation for a long period of time, we studied the change of energy storage modulus under the condition of oscillating strain (1 % Vs 100 %) (Fig. 1(e)). The results show that the ink has a good ability for modulus retention and recovery. Based on the inks with suitable rheological properties, we successfully realized three-dimensional extrusion printing and prepared scaffolds of various sizes for subsequent experiments.

Subsequently, the scaffolds undergo a self-setting process involving low-temperature calcination followed by immersion in PBS. The XRD diffraction pattern (Fig. 2(a)) reveals that the primary phase of the scaffolds transforms from alpha-TCP (PDF#29–0359) to calcium-deficient hydroxyapatite (PDF#09–0432). The transformed scaffolds have sharp diffraction peaks and show high intensity, indicating good crystallinity. This transformation is evidenced by peaks corresponding to P-O stretching vibrations at 1110 cm^{-1} and the disappearance of peaks in the 1500~1200 cm^{-1} range, associated with the F-127 component in the infrared spectra (Fig. 2(b)). A polydopamine coating is then applied to the surface of the CDHA scaffolds using an alkaline-induced self-assembly method. SEM images before and after immersion (Fig. 2(c)) show that the prolonged treatment under alkaline conditions does not change the original structure of the scaffold surface. The uniform distribution of C elements in the EDS spectra (Fig. 2(d)) confirms the formation of a homogeneous coating on the surface. The effects of polydopamine concentration on surface morphology, roughness and contact angle are shown in Fig. 2(e) and (f). The surface of CDHA scaffolds is relatively flat; however, the degree of surface undulation increases with the polydopamine coating. This is evidenced by an increase in measured surface roughness from 10 μm to 20 μm, as shown in Fig. 2(f). However, at higher polydopamine concentrations (6 mg/ml), the coating surface becomes more even, leading to a significant decrease in surface roughness. According to the Wenzel model theory, the contact angle decreased with the increase of roughness on a hydrophilic surface. Therefore, the contact angle in Fig. 2(f) shows an inverse relationship with surface roughness. Despite variations in roughness, the scaffolds retain significant hydrophilic properties, with contact angles below 20°. This hydrophilicity is likely due to the porous structure of CDHA. The micro/nanocrystals at the surface enhance the surface energy, leading to an increased droplet spreading area. Hydrophilic surfaces demonstrate better biocompatibility in physiological conditions, as they exhibit superior adsorption properties for proteins and cells. Finally, leveraging the excellent adsorption properties of the scaffolds, Doxorubicin is loaded by immersing the scaffolds in a Doxorubicin solution. Fig. 2(g) shows the optical change in the scaffolds' color from white to light brown to brownish-red, indicating the formation of a brown polydopamine coating and the adsorption of the red drug Doxorubicin. An encapsulation efficiency of 75.4 % is achieved, minimizing drug loss during the loading process. The negative ζ-potential after encapsulating the PDA coating, as shown in Fig. 2(h), matches values reported in the literature. The observed slight decrease in the

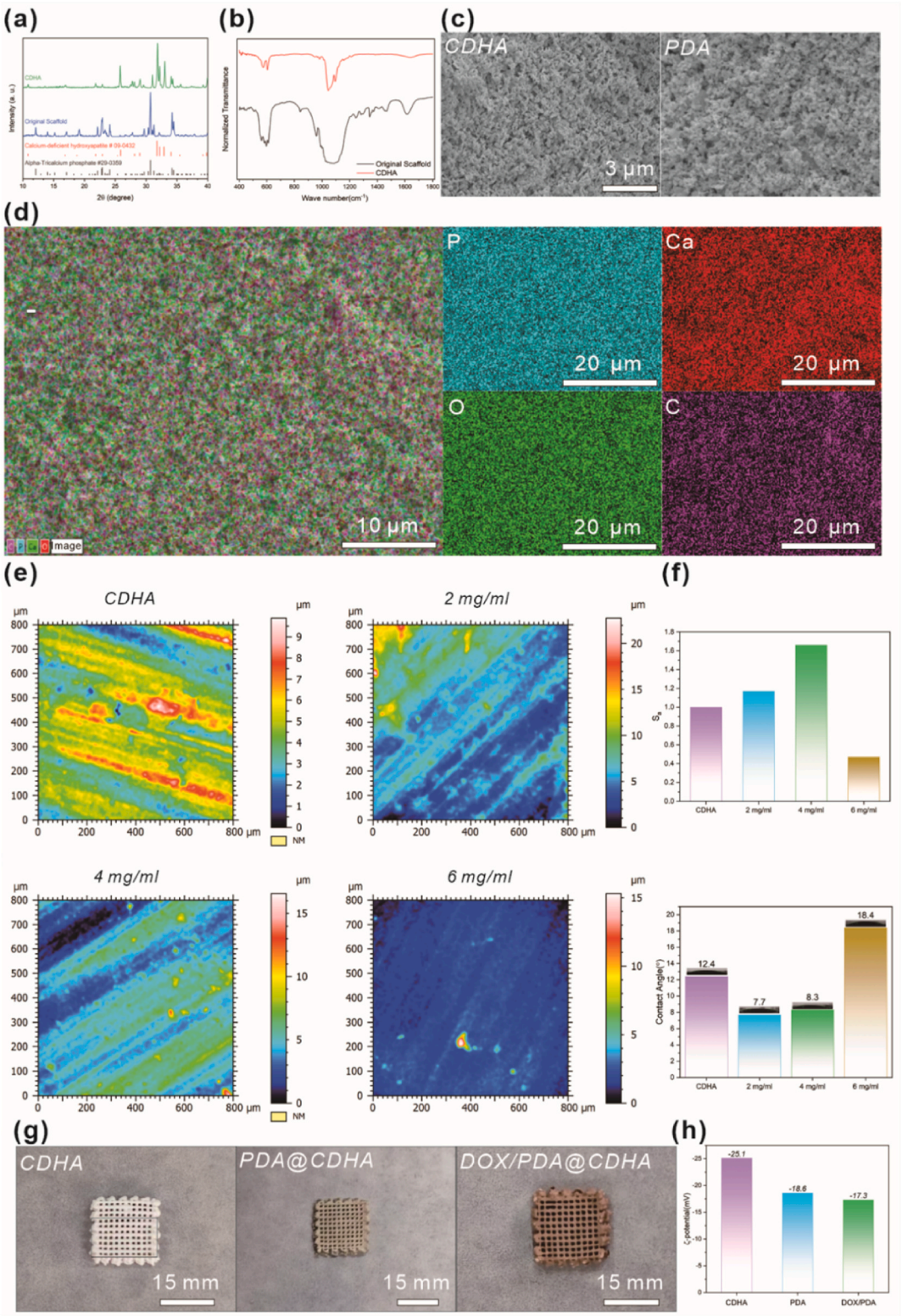

Fig. 2. Characterization of DOX/PDA@CDHA scaffold. XRD pattern (a) and FTIR spectra (b) of original scaffold and Sample CDHA. SEM images (c) of Sample CDHA and PDA. EDS results (d) of Sample PDA. 3D surface morphology images (e), Surface roughness and Water contact angle (f) of Sample CDHA and Samples PDA under different concentration (2 mg/ml, 4 mg/ml, 6 mg/ml).Optical photographs (g) and ζ-potentials (h) of Sample CHDA, PDA@CDHA and DOX/PDA@CDHA.

ζ-potential after Doxorubicin adsorption is due to the interaction with positively charged Doxorubicin molecules, which partially neutralize the scaffold's surface charge.

3.2. Antitumor-related properties of DOX/PDA@CDHA scaffold (photothermal and doxorubicin release properties)

We designed synergistic a photothermal and chemotherapeutic antitumor treatment using PDA coating and DOX release. On the one hand,

The coating content is controlled by varying the dopamine solution concentration, allowing for tailored photothermal performance. Fig. 3 (a) demonstrates that the photothermal efficiency of the scaffolds positively correlates with the polydopamine concentration at a constant laser power (1 W/cm^2). A dopamine concentration of 4 mg/ml is valid for the scaffolds to provide efficient thermotherapy temperature (>48 °C). Fig. 3(b) shows that varying laser power affects the photothermal performance of the scaffold, with equilibrium temperature rising with increased power density. This indicates that the photothermal performance of the PDA@CDHA scaffold can be precisely controlled by adjusting both the polydopamine content and the laser power density. Fig. 3(c) indicates that the photothermal conversion efficiency of the scaffold is 19.13 %. Compared with the high photothermal efficiency of PDA, significant decrease of the efficiency comes from the CDHA scaffold which has no obvious photothermal performance under NIR. Fig. 3 (d) shows that the scaffold's photothermal performance remains stable over multiple cycles, indicating robust cyclic stability. Additionally, rapid DOX release at the tumor site is triggered by both near-infrared (NIR) irradiation and acidic pH conditions. Fig. 3(e) and (f) illustrate how both the surrounding medium's pH and the temperature influence DOX's release kinetics. It could be validated that DOX has a higher release capacity under acidic conditions and a short period of NIR irradiation achieves a significant burst release effect, resulting in sufficient DOX concentration around the tumor site for a longer period of time. These results demonstrate that the DOX@PDA-CDHA scaffold offers excellent photothermal conversion performance and localized, susutained release of chemotherapeutic drug DOX, establishing a strong foundation of synergistic photothermal and chemotherapeutic anti-tumor treatment in vitro and in vivo.

3.3. *In vitro anti-tumor performance of DOX/PDA@CDHA scaffold under NIR laser excitation*

Building on the previously outlined photothermal properties, which enable localized heat generation under NIR laser excitation, and controlled drug release capabilities, we investigate the effects of the scaffold on the proliferation, apoptosis, migration and invasion of MG63 and HOS tumor cells under NIR laser excitation at the in vitro cellular level. The sample designation and abbreviation are listed in Table 1. The cell activity test in Fig. S1 assesses the effect of treatment conditions (laser power and irradiation time) on the anti-tumor performance of the scaffolds. As expected, tumor cell activity decreases significantly with increasing laser power and irradiation time. However, laser power exceeding 1.5 W/cm^2 might be harmful to normal tissues [41]. After balancing efficacy and safety, we selected 1 W/cm^2 for 5 min as the treatment condition, ensuring effective tumor targeting while

Table 1
Sample designation and abbreviation.

Sample name	Scaffold used	With or without NIR
Sample CDHA	CDHA	Without
Sample PDA	PDA@CDHA	Without
Sample PDA + NIR	PDA@CDHA	With
Sample DOX/PDA	DOX/PDA@CDHA	Without
Sample DOX/PDA + NIR	DOX/PDA@CDHA	With

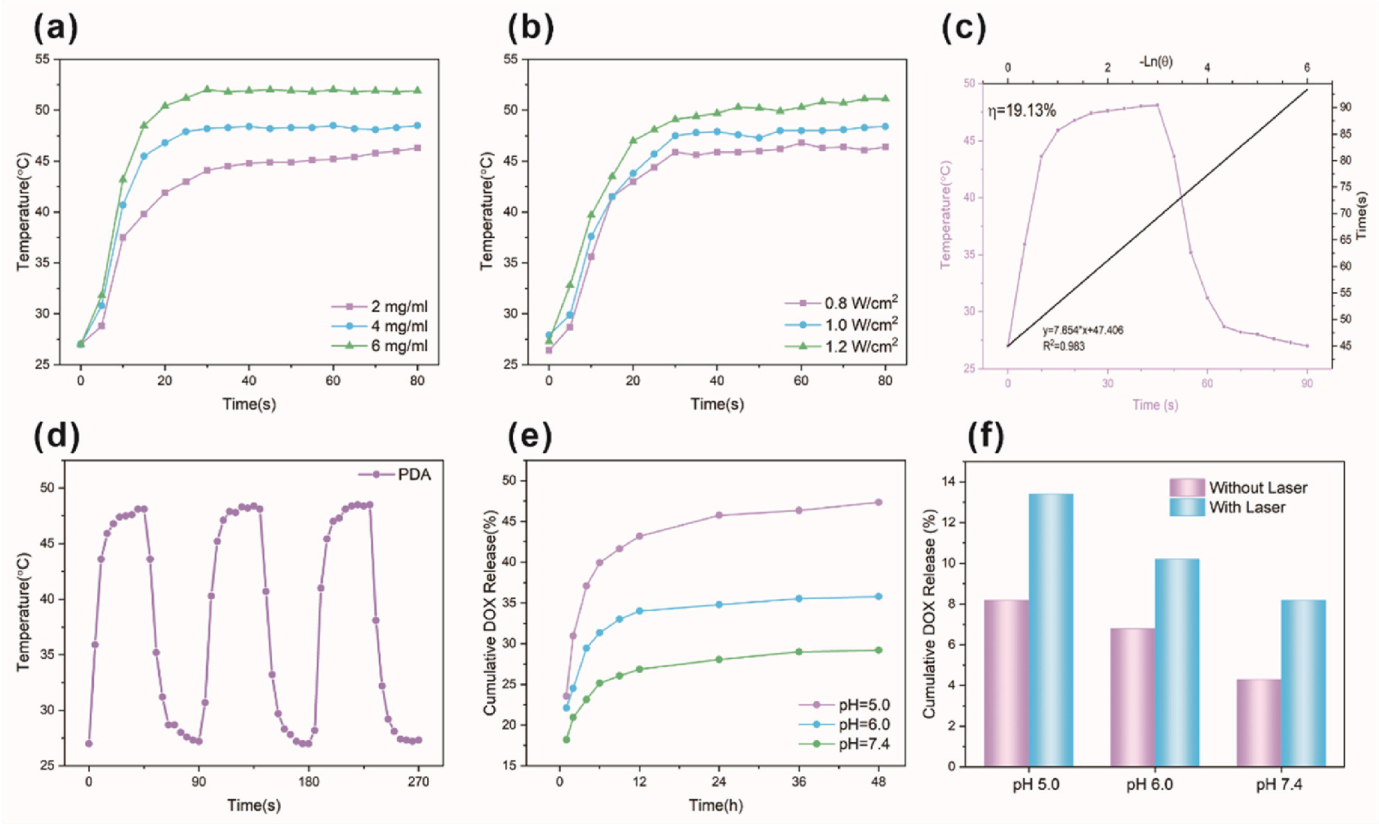

Fig. 3. Photothermal properties and DOX release properties of DOX/PDA@CDHA scaffold. Photothermal-conversion curves (a) of Samples PDA under different polydopamine concentration (2 mg/ml, 4 mg/ml, 6 mg/ml) when illuminated by an 808 nm laser with a power density of 1.0 W/cm^2. Photothermal-conversion curves (b) of Samples PDA under different power densities (0.8 W/cm^2, 1.0 W/cm^2, 1.2 W/cm^2) under polydopamine concentration of 4 mg/ml. Heating and cooling curves of Sample PDA (4 mg/ml, 1.0 W/cm^2), and the linear fitting curve of time and -Ln (θ) acquired from the cooling period(c). Photothermal-conversion curves of Sample PDA (4 mg/ml, 1.0 W/cm^2) under three "on-off'' cycles of NIR laser exposure (d). Cumulative release of DOX under different treatments: different pH values (e) and with/without Laser (f).

minimizing potential damage to surrounding healthy tissues. The effect of the multifunctional scaffold on the activity of MG63 and HOS cells is evaluated. As shown in Fig. 4(a), Scaffold PDA@CDHA has no significant inhibitory effect on tumor cell growth. In contrast, Scaffold DOX/PDA@CDHA under NIR laser excitation (Sample DOX/PDA + NIR) showed a significantly lower OD value (0.19 ± 0.03 for MG63 and 0.24 ± 0.01 for HOS) compared to single treatments, either photothermal therapy (Sample PDA + NIR, 0.86 ± 0.04 for MG63 and 0.80 ± 0.01 for HOS) or chemotherapy (Sample DOX/PDA, 0.21 ± 0.02 for MG63 and 0.29 ± 0.01 for HOS), confirming the superiority of synergistic treatment. Staining of live and dead cells based on Calcein Acetoxymethyl Ester (Calcein-AM) and Propidium Iodide (PI) (Fig. 4(b)) corroborates the above observations. Intense green fluorescence, indicating live cells, predominates in the Sample PDA, whereas the Sample DOX/PDA + NIR shows significantly increased red fluorescence, signaling greater tumor cell death. Additionally, flow cytometry quantifies apoptosis, revealing enhanced cell death due to the synergistic photothermal and chemotherapeutic mechanisms in Sample DOX/PDA + NIR (Fig. 4(c)). The percentage of apoptotic cells is significantly smaller in the Sample PDA than in other groups, meaning lower cytotoxicity of the original scaffolds. Apoptosis induced by chemotherapy (Sample DOX/PDA) and photothermal therapy (Sample PDA + NIR) results in a higher apoptosis rate on Sample DOX/PDA + NIR, consistent for both HOS and MG63. It is widely accepted that photothermal/chemotherapeutic synergistic treatment of the scaffold not only affects tumor cells directly adsorbed on the surface of the scaffold, but also induces significant apoptosis in tumor cells near by and away from the scaffold.

To further validate the anti-tumor performance of DOX/PDA@CDHA, the gene expression of apoptosis-related genes Bcl-2, Bax, Caspase 8 and Caspase 3 is monitored by qRT-PCR after 3 days of culture

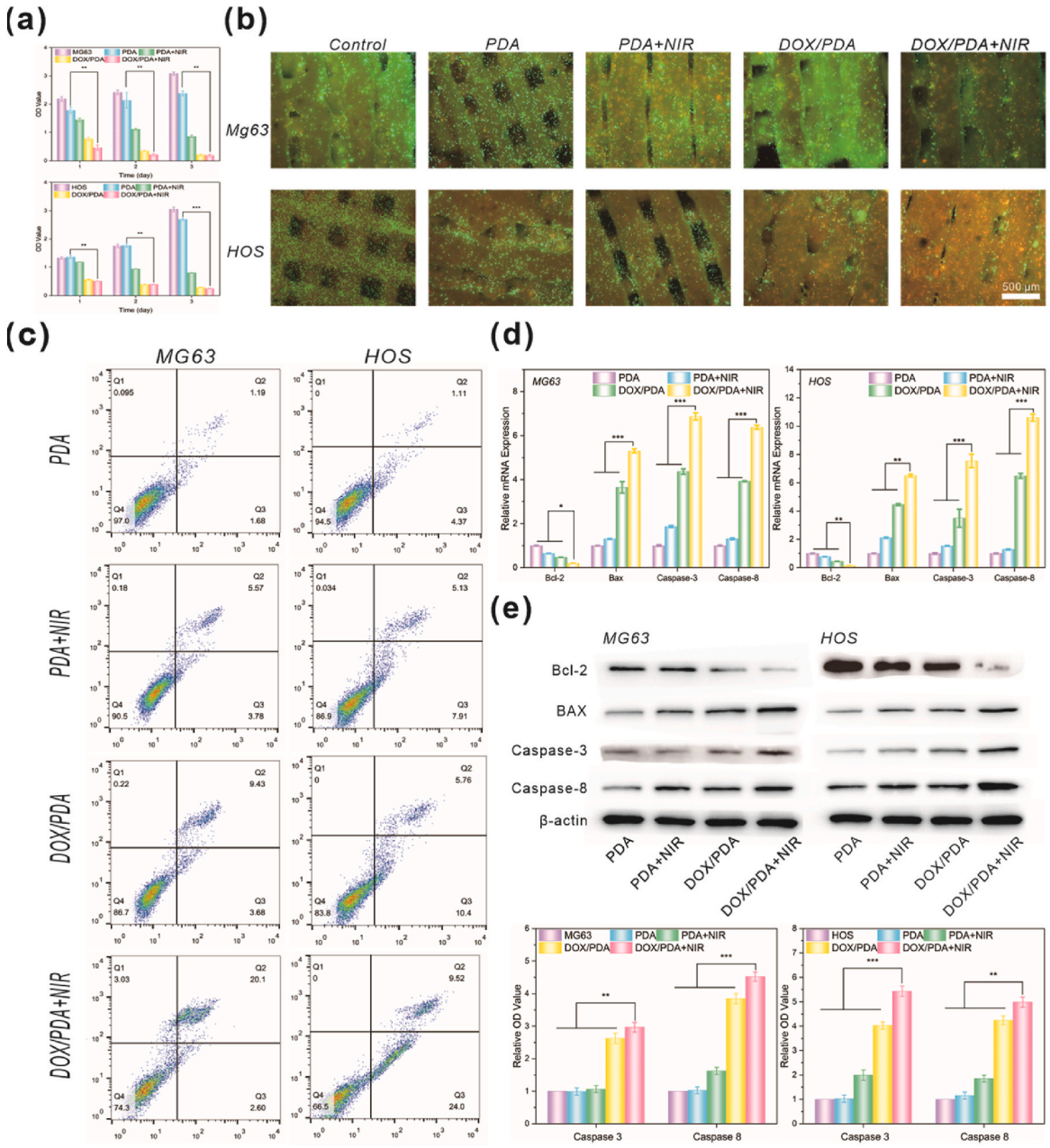

Fig. 4. In vitro antitumor effect of DOX/PDA@CDHA scaffold. Cellular viability (a), images of live/dead staining (b), and cellular apoptosis profiles(c), RT-PCR results (d) and Western plot analysis (e) of apoptosis-related genes (Bcl-2, Bax, Caspase 8 and Caspase 3) and apoptosis-related proteins (Caspase 8 and Caspase 3) concentration (f) of MG63 and HOS cells under different treatments (Samples PDA and DOX/PDA with or without NIR). (*$p < 0.05$, **$p < 0.01$ and ***$p < 0.001$).

(Fig. 4(d)). Bcl-2 is known for its role in inhibiting apoptosis, whereas Bax promotes apoptosis, counteracting Bcl-2. Caspase 8 protein, located in the upstream of the apoptosis cascade reaction, is responsible for initiating the downstream caspase protease. Caspase 3 protein, as the most critical executor of the downstream of the cascade reaction, performs the role of shearing the cellular structural proteins, which directly lead to apoptosis. The results point out that Sample DOX/PDA + NIR significantly decreases the apoptosis inhibiting gene bcl-2 (0.19 ± 0.01 for MG63 and 0.24 ± 0.01 for HOS), while the pro-apoptosis gene bax (5.3 ± 0.1 for MG63 and 0.14 ± 0.01 for HOS) and both caspase 3 (6.51 ± 0.09 for MG63 and 7.54 ± 0.47 for HOS)and caspase 8 (6.37 ± 0.1 for MG63 and 10.6 ± 0.24 for HOS), which are involved in the apoptosis cascade reaction, are significantly increased. To further confirm the expression of these factors in protein level, Western plot assay were also performed. In agreement with the qRT-PCR results, Sample DOX/PDA + NIR downregulates the expression of Bcl-2 protein and upregulates the expression of BAX, Caspase 3 and Caspase 8 to the greatest extent among all samples in the case of MG63 and HOS (Fig. 4(e)). Additionally, the levels of apoptosis-related Caspase 3 and Caspase 8 are assessed using commercially available Caspase 3 and Caspase 8 activity detection kits, according to the manufacturer's instructions (Fig. 4(f)). The apoptotic gene protein contents are significantly elevated in Sample DOX/PDA + NIR, which combines the two therapeutic treatments (photothermal and chemotherapeutic), corroborating the gene expression results.

In addition to in-situ proliferation, tumor development also involves invasion and migration. Earlier research suggest that the unique microenvironment of bone tissue makes it susceptible to exogenous tumor cell invasion [41,42]. Tumor cells must penetrate the basement membrane to invade surrounding tissues. This paper utilizes the Transwell invasion assay to simulate the process of cell invasion. Under

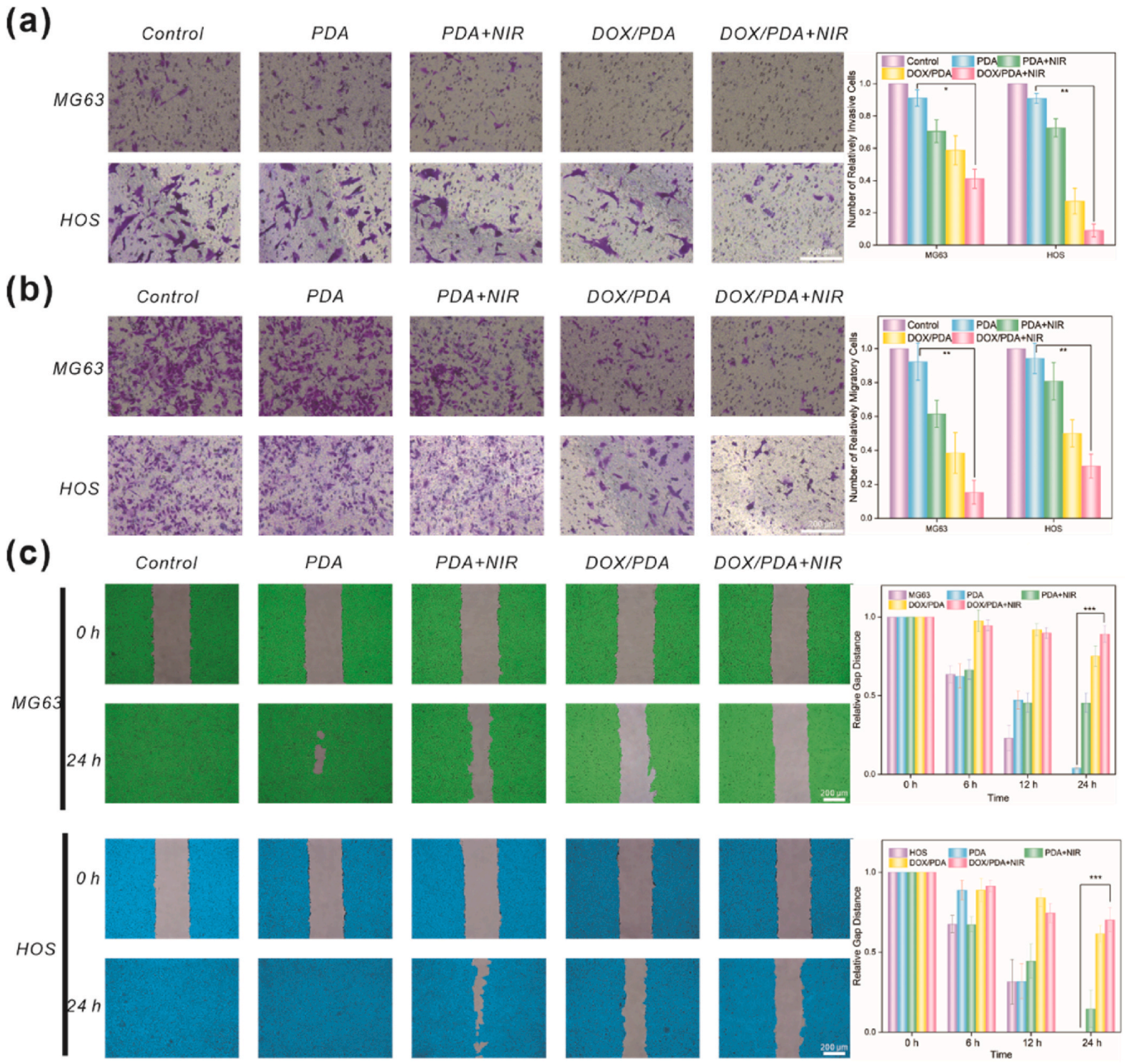

Fig. 5. In vitro antitumor effect of DOX/PDA@CDHA scaffold. Transwell invasion assay and quantitative analysis (a), Transwell migration assay and quantitative analysis (b) and scratch healing assay and quantitative analysis (c) of MG63 and HOS cells under different treatments (Samples PDA and DOX/PDA with or without NIR). (*$p < 0.05$, **$p < 0.01$ and ***$p < 0.001$).

identical experimental conditions (Fig. 5(a)), the Sample DOX/PDA + NIR exhibited the lowest number of cells penetrating the basement membrane. Quantitative statistical analysis (0.41 ± 0.06 for MG63 and 0.09 ± 0.04 for HOS) further demonstrates that synergistic anti-tumor effectively inhibits the invasion of both types of tumor cells. After invasion, the tumor cells often enter the bloodstream and migrate. In this paper, the effects of the scaffold on the migration ability of tumor cells are assessed using the Transwell migration assay and the scratch healing assay, and the results are shown in Fig. 5(b) and (c) and Fig. S2. The smallest number of cells in the Sample DOX/PDA + NIR is shown in Fig. 5(b) and supported by quantitative analysis (0.15 ± 0.07 for MG63 and 0.31 ± 0.08 for HOS), indicating a significant inhibitory effect on the migration of tumor cells. The results of the scratch healing assay are presented in Fig. 5(c) and Fig. S2. On the PDA@CDHA scaffold, cell scratches gradually narrow with time and partially (MG63) or completely (HOS) close after 24 h, suggesting that the native scaffolds are less effective at inhibiting tumor cell migration. In contrast, the scratches on the Sample DOX/PDA + NIR remain wider after 24 h. Quantitative statistical analyses on the right side shows that the photothermal/chemotherapeutic synergy (0.89 ± 0.06 for MG63 and 0.71 ± 0.08 for HOS) significantly hinders tumor cell migration. Overall, the prepared DOX/PDA@CDHA scaffold demonstrates effective anti-tumor

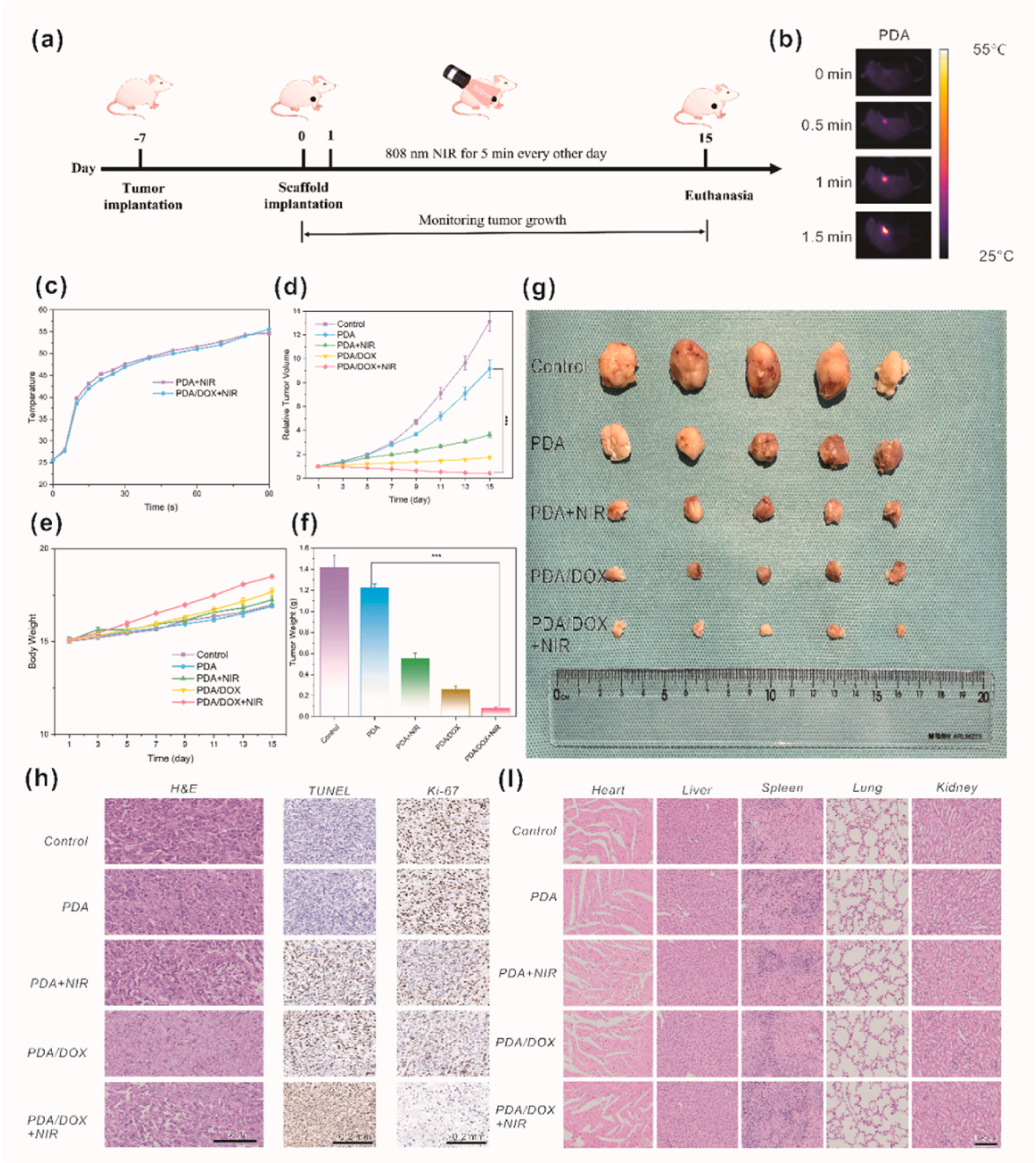

Fig. 6. In vivo antitumor effect of DOX/PDA@CDHA scaffold. Schematic presentation (a) of the photothermal treatment process. Infrared thermal images (b) and Photothermal-conversion curves (c) of tumor sites in the tumor-bearing mice of the Sample PDA + NIR and DOX/PDA + NIR. Relative tumor volumes (d) and Body weights (e) curves of tumor-bearing mice during the treatment. The Optical photographs (f) and final weights (g) of tumor of different groups after the 14-day treatment.Histological analysis (H&E, TUNEL and Ki-67 staining) of tumor sections collected from different groups (h). H&E staining of the major organs harvested from different groups (i). (*$p < 0.05$, **$p < 0.01$ and ***$p < 0.001$).

performance in vitro, providing a solid foundation for subsequent in vivo experiments.

3.4. In vivo anti-tumor performance of DOX/PDA@CDHA scaffold under NIR laser excitation

The promising in-vitro anti-tumor performance of DOX/PDA@CDHA scaffold provides the basis for subsequent in vivo experiments. The treatment process is conducted for tumor-loaded nude mice as in Fig. 6 (a). The tumor-bearing nude mice are randomly divided into five groups: Group 1 (blank control), Group 2 (Sample PDA), Group 3 (Sample PDA + NIR), Group 4 (Sample DOX/PDA) and Group 5 (Sample DOX/PDA + NIR). When the tumors reach to a predetermined volume, the scaffolds are implanted by making an incision at the edge of the tumors. Real-time thermal imaging of the tumor area is captured using an infrared imager. The tumor area implanted with the DOX/PDA@CDHA scaffold rapid warms under 808 nm laser irradiation (1 W/cm^2, 5 min), reaching and maintaining a temperature $\geq$50 °C, which is optimal for effective thermotherapy. (Fig. 6(b)). In addition, the temperature gradient field around the tumor tissues in the figure shows that the heat ablates the tumor tissues while minimizing the damage to the normal tissues. The real-time temperature profiles in Fig. 6(c) indicate that the experimental scaffolds achieve sufficient thermotherapy temperatures in a short period. The results of the relative tumor volume within 14 days (Fig. 6 (d)) shown significant atrophy ($p < 0.001$) in the Sample DOX/PDA + NIR, which exhibited the best tumor suppression rate compared to single photothermal therapy (Sample PDA + NIR) or chemotherapy (Sample DOX/PDA). These conclusions are further validated by the weighing results (Fig. 6(f), Sample DOX/PDA + NIR 0.08 ± 0.01 Vs Sample PDA 1.22 ± 0.04) and optical photographs (Fig. 6(g) and Fig. S3) of all tumors dissected from the mice at the end of the experiment. To further assess cell morphology, apoptosis, and proliferation, hematoxylin and eosin (H&E) staining, deoxynucleotidyl transferase uridine triphosphate engraved-needle end-labeling (TUNEL) staining and Ki-67 staining are used to stain tumors in different treatment groups (Fig. 6(h)). Different degrees of apoptosis and necrosis of tumor cells appear in all the experimental groups and obvious nuclear condensation and fragmentation could be observed in H&E staining of the Sample DOX/PDA + NIR. Apoptosis is the highest in TUNEL images, but cell proliferative activity was the lowest in Ki-67 images, in contrast. The aforementioned phenomena demonstrate the photothermal/chemotherapeutic synergistic antitumor properties in vivo. It is well known that dose-cumulative cardiotoxicity is the greatest limitation of DOX application, and residual drugs could enter the blood circulation after treatment and be metabolized by the liver and partially excreted by the kidneys. During the treatment cycle of up to 14 days, no significant changes in body weight are detected in all groups of mice (Fig. 6(e)), indicating that the treatment regimen has minimal side effects on mice. H&E staining of heart, spleen, lung and kidney tissues highlights intact and tightly arranged cells with no tissue fragmentation, emphasizing that the topical treatment has no toxic side effects on these tissues and organs (Fig. 6(i)). Thus, the prepared DOX/PDA@CDHA scaffold and the corresponding treatment procedure can effectively ablate tumors at lower drug doses with no side effects on normal tissues, making it a strong candidate for local antitumor treatment.

3.5. In vitro osteogenic performance of PDA@CDHA scaffold

As described in the introduction, postoperative bone tumor sites must address both bone regeneration and tumor suppression. Besides inhibiting tumor growth, the scaffolds should have the function of promoting osteogenic properties at the medium/long-term level. Therefore, BMSCs are selected to study the osteogenic properties of the PDA@CDHA scaffold. BMSCs are more numerous on the scaffold surface with good morphology and uniform spreading, indicating that the scaffolds' surface properties and composition are conducive to the adhesion, proliferation and osteogenic differentiation of BMSCs (Fig. 7 (a) and Fig. S4). Compared with Sample CDHA, Sample PDA presents similar cell proliferation ability (Fig. 7(b)). The bright green color affiliated with living cells confirms good cell activity in Fig. 7(a). Other researchers have similarly observed that that dopamine coating on the surface of calcium phosphate scaffolds promoted the proliferation of osteoblasts in a concentration-dependent manner [43]. To further validate the osteogenic performance of PDA@CDHA, the gene expression of osteogenic-related genes ALP, RUNX2 and OPN is monitored by qRT-PCR (Fig. 7(c)) and WB assay (Fig. 7(d)). ALP, a marker of early osteogenic differentiation, is regarded as a representative gene related to osteogenesis. RUNX2, a major transcription factor for osteogenic differentiation of stem cells, is a central control gene for osteoblast phenotype. OPN, effectively stimulating osteoclastic genesis/resorption, is closely related to bone formation and development. The treatment of Sample PDA@CDHA could effectively upregulate the level of ALP, RUNX2 and OPN mRNAs and proteins in BMSCs. Flow cytometry (Fig. 7 (e)) is used to quantify apoptosis mediated by scaffolds. There is no statistical difference among Sample Control, CDHA and PDA, further proving the cellular activity. Alkaline phosphatase (ALP) is the most widely recognized marker of osteoblast activity. Triggering crystal nucleation of extracellular matrix calcium deposits through hydrolysis of a variety of phosphate compounds which in turn affects Pi homeostasis, this specific protein is a hallmark product of the early stage of the osteoblast phenotype. The early osteogenic activity of scaffolds is assessed using alkaline phosphatase (ALP) staining and quantified with ALP activity assay kits, following manufacturer protocols. Fig. 7(f) shows the ALP staining results of each scaffold after 7 days of co-culture with BMSC cells. As marked from the results, the ALP activity of the Sample PDA group is significantly increased and its staining is gradually deepened compared with the control group. The ALP activity on the surface of the scaffolds is further investigated by the ALP quantitative detection kit, as shown in Fig. 7(g). The results show that the ALP activity of the Sample PDA is the highest on the seventh day and such results are generally consistent with the ALP staining results. The two cross-corroborative results exhibited that the surface polydopamine coating could increase the ALP activity of BMSC cells, which thereby promoted their osteogenic differentiation and bone matrix formation. Mineralization nodules are important markers for the end stage of osteogenic differentiation. The effect of scaffolds on the in vitro mineralization ability of BMSCs is investigated by Alizarin Red S (ARS) staining. The results, as discovered in Fig. 7(h), show that large red mineralized nodules are visible in the PDA group, confirming that the polydopamine coating could promote the formation of calcium nodules in vitro. While these findings are promising for the PDA@CDHA scaffold's bone regeneration capabilities, further in vivo studies are necessary to evaluate its long-term osteogenic potential and biocompatibility in a physiological environment.

3.6. In vitro angiogenic properties of PDA@CDHA scaffold

One of the reasons why critical bone defects could not realize self-repairing is that the vascular bridging between the broken ends is often limited, resulting in insufficient nutrients at the defect site [44]. In addition, numerous studies have shown that the vascularization of bone tissues and bone regeneration is a mutually coupled process [45–47]. Besides providing transport pathways for the necessary nutrients and metabolic waste, the vasculature also contains the special cell populations secreting factors to promote bone repair. HUVECs are utilized to study their adhesion, proliferation, and angiogenic capacity, key factors in angiogenesis, to characterize the angiogenic properties of the scaffolds. As shown in Fig. 8(a) and Fig. S5, HUVECs adhere well to the scaffolds with narrow cell morphology, tight intercellular connections and large spreading area, which suggests the scaffold's gradient pore structure and surface veneer of the scaffolds are favorable for the pre-adhesion and proliferation of HUVECs. Compared with Sample

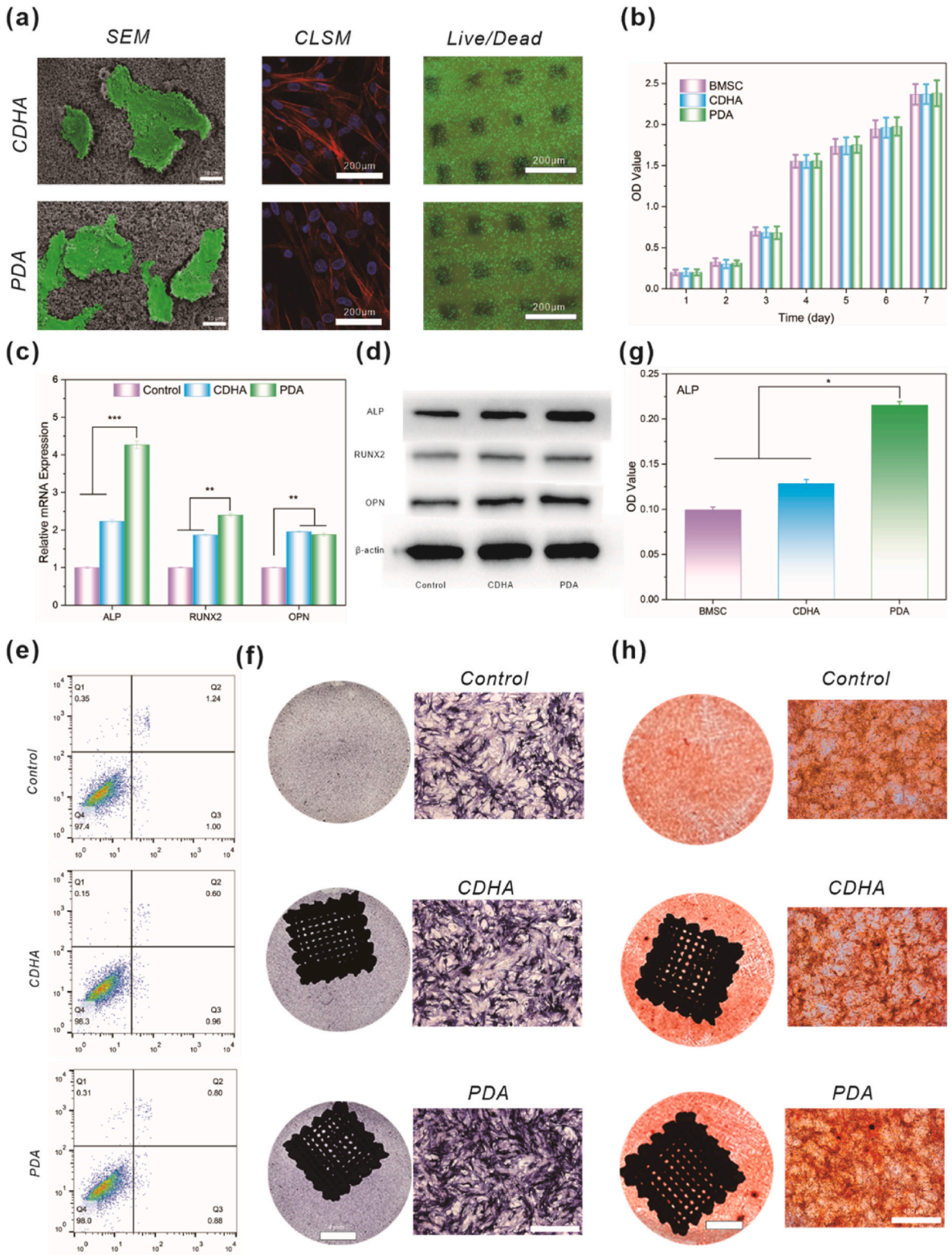

Fig. 7. In vitro osteogenic performance of PDA@CDHA scaffold. Adhesion and morphology using SEM, Cytoskeleton/nucleus staining and Live/dead staining of BMSCs from different groups (a). Cellular viability(b), qRT-PCR results (c) and Western plot analysis (d) of osteogenic-related genes (ALP, RUNX2 and OPN), cellular apoptosis profiles (e), ALP staining (f) ALP protein concentration(g) and ARS staining (h) of BMSCs from different groups. (*$p < 0.05$, **$p < 0.01$ and ***$p < 0.001$).

CDHA, Sample PDA manages similar cell proliferation ability as shown in Fig. 8(b). The bright green color representative of live cells in Fig. 8(a) also corroborates the good cell activity. To further validate the angiogenic performance of PDA@CDHA, the expression of osteogenic-related factor VEGF and CD31 is monitored by qRT-PCR (Fig. 8(c)) and WB assay (Fig. 5(e)). VEGF could modulate vascular permeability and promote cell migration, proliferation and survival during neovascularization.CD31 immunoglobulin molecule, is the key factor involved in platelet adhesion and aggregation. The treatment of Sample PDA could effectively upregulate the level of VEGF and CD-31 mRNAs

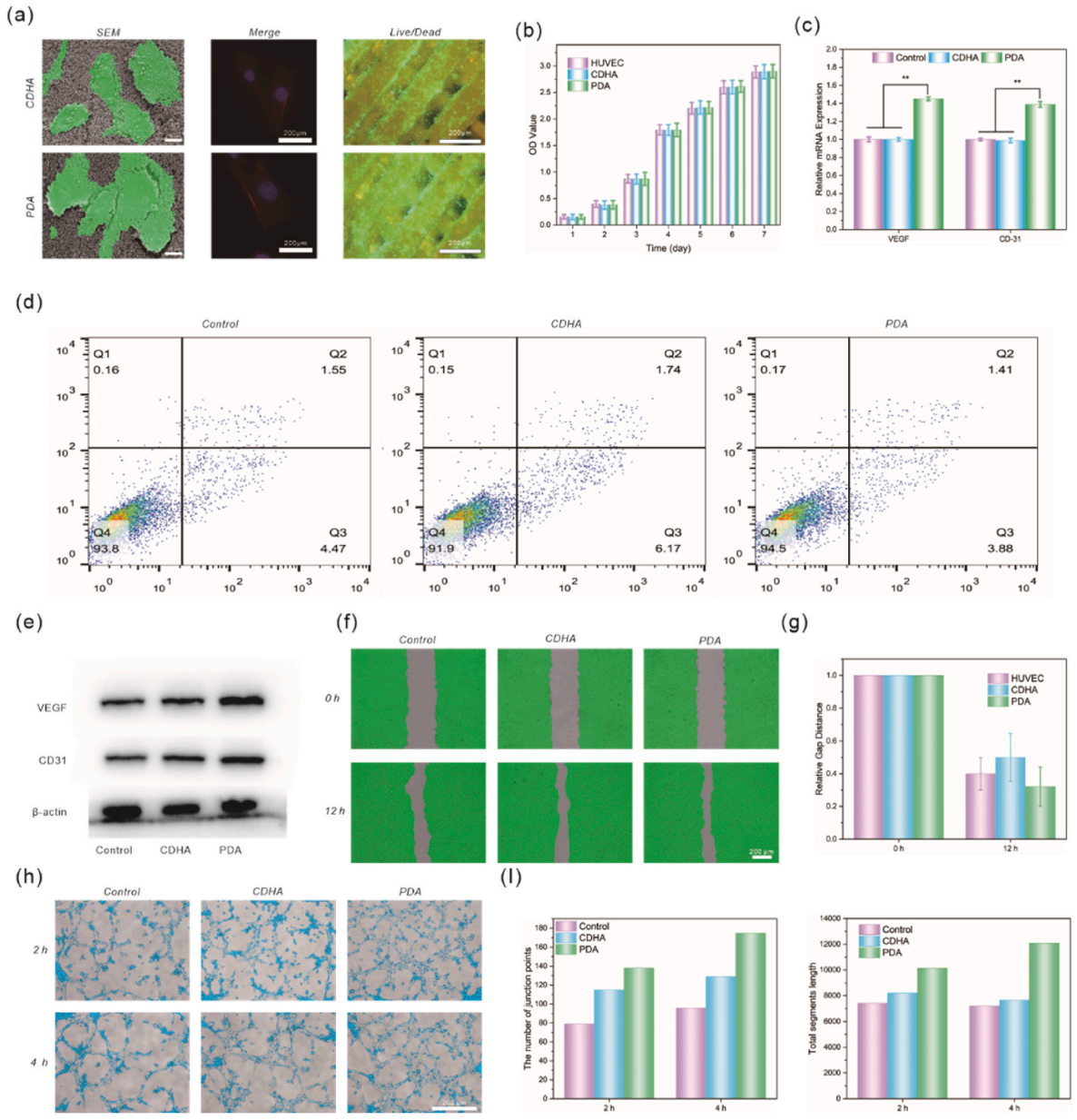

Fig. 8. In vitro angiogenic performance of PDA@CDHA scaffold. Adhesion and morphology using SEM, Cytoskeleton/nucleus staining and Live/dead staining of HUVECs from different groups (a). Cellular viability(b), RT-PCR results (c) and Western plot analysis (d) of angiogenic-related genes (VEGF and CD31), cellular apoptosis profiles (e), scratch healing assay (f) and quantitative analysis (g), blood vessel formation experiment (h) and its quantitative analysis of junction points and segments length (i) of HUVECs from different groups. (*$p < 0.05$, **$p < 0.01$ and ***$p < 0.001$).

and proteins in HUVECs. Flow cytometry (Fig. 8(d)) is used to quantify apoptosis mediated by scaffolds. There is no statistical difference among Sample Control, CDHA and PDA, further indicating the cellular activity. The cell scratch assay (Fig. 8(f)) and quantitative analysis results (Fig. 8 (g)) show that the number of migrated cells in the Sample PDA is significantly increased compared with that in the Sample CDHA, indicating that the polydopamine coat on the surface is able to promote the migration of HUVECs. In the blood vessel formation experiment (Fig. 8 (h)) and its quantitative analysis (Fig. 8(i)), the HUVECs of each group gradually migrate, arrange and form bifurcation or reticulation after 2 h of culture. As the time further extends (4h), the tubular network of each group has increased, but the PDA group always maintains a certain advantage. Quantitative analysis results show that the number of junction points and total segment length of the tubular network in the Sample PDAs relatively higher than other groups. The above results suggest that Sample PDA favors the formation of blood tubules. In conclusion, the PDA@CDHA scaffold demonstrates promising angiogenic properties, indicating its potential to enhance revascularization and thereby improve bone regeneration performance.

3.7. *In vivo osteogenic properties of PDA@CDHA scaffold*

The bone regeneration ability of Sample PDA@CDHA is further investigated by using 5 mm rat bone defect model. The bone recovery at week 8 was evaluated using micro-CT and histological analysis(Fig. 9). Compared with the Control, Sample CDHA and PDA have more new bone in growth, indicating the excellent osteoinductive properties of calcium phosphates, while the Sample PDA@CDHA has the best effect on new bone in growth among the three groups, The results of quantitative analysis of the newly formed bone tissue showed that the BMD, BV/TV, Tb.Th and Tb.N of the newly formed bone at Sample PDA@CDHA were significantly higher than the control group, in some

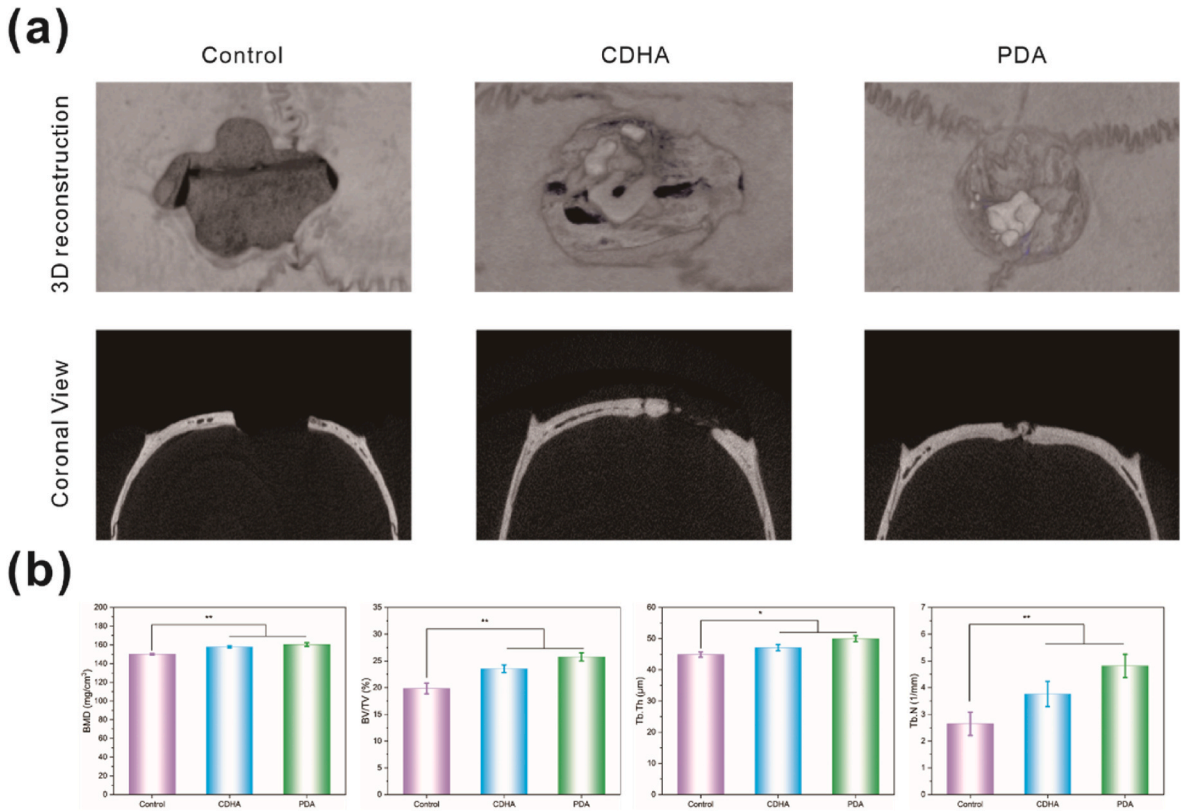

Fig. 9. In vivo osteogenic performance of PDA@CDHA scaffold. Representative micro-CT reconstruction images of 3D (a) and coronal view in different groups at week 8 post-surgery. Micro-CT quantification: BMD (a); BV/TV (b); Tb.Th (c) and Tb.N (d).

cases even the Sample CDHA. The differences could result from the better angiogenic property of Sample CDHA. Such results further confirm the potential application in bone regeneration of PDA@CDHA scaffold.

4. Conclusion

Collectively, a multifunctional therapeutic platform for the synergistic treatment of osteosarcoma is constructed by applying a polydopamine coating to the surface of 3D printed CDHA porous scaffolds while achieving a locally stimulated, controlled slow release of DOX at the tumor site. The porous CDHA scaffolds with good bone regeneration properties are coated with polydopamine, known for bioactive and photothermal properties, followed by the in-situ adsorption of the chemotherapeutic drug DOX. This combination enables the composite scaffold to exert antitumor effects through a synergy between photothermal therapy and chemotherapeutic action. In addition, the polydopamine-coated CDHA scaffolds enhance osteogenic and angiogenic performance in vitro and in vivo, thus enhancing the bone regeneration after osteosarcoma resection. Our study demonstrates that CDHA scaffolds coated with polydopamine and subsequently loaded with DOX in situ have excellent osteosarcoma treatment and osteogenic and angiogenic capabilities, offering a promising multifunctional material system for the regeneration of bone tissues following osteosarcoma resection, with potential applications in other areas of bone disease treatment.

CRediT authorship contribution statement

Lu Wang: Writing – original draft, Visualization, Project administration, Methodology, Data curation, Conceptualization. **Zihan Dai:** Writing – original draft, Visualization, Project administration, Methodology, Data curation, Conceptualization. **Jianqiang Bi:** Writing – review & editing, Supervision, Project administration, Funding acquisition, Conceptualization. **Yunzhen Chen:** Writing – review & editing, Supervision, Project administration, Funding acquisition, Conceptualization. **Ziyu Wang:** Visualization, Validation, Supervision, Investigation, Formal analysis, Conceptualization. **Zhenqian Sun:** Writing – review & editing, Software, Methodology, Investigation, Data curation. **Zhongjie Ji:** Writing – review & editing, Validation, Software, Methodology, Data curation. **Hongliang Wang:** Writing – review & editing, Visualization, Software, Resources, Investigation, Data curation. **Yan Zhang:** Visualization, Methodology. **Limei Wang:** Visualization, Methodology. **Junjie Mao:** Visualization, Software, Resources, Formal analysis. **Junxing Yang:** Visualization, Software, Resources, Investigation, Data curation.

Declaration of competing interest

We declare that we do not have any commercial or associative interest that represents a conflict of interest in connection with the work submitted.

Data availability

Data will be made available on request.

Acknowledgment

This work was supported by the Key R&D Program of Shandong Province (2023CXGC010305) and The Special Fund for Leading Talent in Mount Tai of Shandong Province. We thank the Translational Medicine Core Facility of Shandong University, Laboratory of Basic Medical Sciences of Qilu Hospital of Shandong University, Center for Experimental Nuclear Medicine & Electron Microscope, School of Basic Medical Sciences, Shandong University for consultation and instrument availability that supported this work. We would like to thank Shiyanjia

Lab (www.shiyanjia.com) for instrument availability.

Appendix A. Supplementary data

Supplementary data to this article can be found online at https://doi.org/10.1016/j.mtbio.2024.101253.

References

[1] Y. Wu, M. Cheng, Y. Jiang, X. Zhang, J. Li, Y. Zhu, Q. Yao, Calcium-based biomaterials: unveiling features and expanding applications in osteosarcoma treatment, Bioact. Mater. 32 (2024) 385–399, https://doi.org/10.1016/j.bioactmat.2023.10.008.

[2] S. Li, H. Zhang, J. Liu, G. Shang, Targeted therapy for osteosarcoma: a review, J. Cancer Res. Clin. Oncol. 149 (2023) 6785–6797, https://doi.org/10.1007/s00432-023-04614-4.

[3] C. Feng, Y. Jiang, T. Wang, D. Tian, C. Shen, Y. Wang, H. Qian, Recent advances on nanostructured biomaterials in osteosarcoma treatment, Coord. Chem. Rev. 493 (2023) 215315, https://doi.org/10.1016/j.ccr.2023.215315.

[4] J. Gill, R. Gorlick, Advancing therapy for osteosarcoma, Nat. Rev. Clin. Oncol. 18 (2021) 609–624, https://doi.org/10.1038/s41571-021-00519-8.

[5] H. Tian, J. Cao, B. Li, E.C. Nice, H. Mao, Y. Zhang, C. Huang, Managing the immune microenvironment of osteosarcoma: the outlook for osteosarcoma treatment, Bone Res 11 (2023) 11, https://doi.org/10.1038/s41413-023-00246-z.

[6] B. Wen, Y.-t. Wei, K. Zhao, The role of high mobility group protein B3 (HMGB3) in tumor proliferation and drug resistance, Mol. Cell. Biochem. 476 (2021) 1729–1739, https://doi.org/10.1007/s11010-020-04015-y.

[7] Y. Liu, Q. Li, Q. Bai, W. Jiang, Advances of smart nano-drug delivery systems in osteosarcoma treatment, J. Mater. Chem. B 9 (2021) 5439–5450, https://doi.org/10.1039/d1tb00566a.

[8] C. Sun, S. Li, J. Ding, Biomaterials-boosted immunotherapy for osteosarcoma, Adv. Healthcare Mater. (2024) 2400864, https://doi.org/10.1002/adhm.202400864.

[9] C. Wang, Z. Ma, K. Yuan, T. Ji, Using scaffolds as drug delivery systems to treat bone tumor, Nanotechnology 33 (2022) 212002, https://doi.org/10.1088/1361-6528/ac5017.

[10] H. Tian, R. Wu, N. Feng, J. Zhang, J. Zuo, Recent advances in hydrogels-based osteosarcoma therapy, Front. Bioeng. Biotechnol. 10 (2022) 1042625, https://doi.org/10.3389/fbioe.2022.1042625.

[11] Y. Wang, H. Zhang, H. Qiang, M. Li, Y. Cai, X. Zhou, Y. Xu, Z. Yan, J. Dong, Y. Gao, C. Pan, X. Yin, J. Gao, T. Zhang, Z. Yu, Innovative biomaterials for bone tumor treatment and regeneration: tackling postoperative challenges and charting the path forward, Adv. Healthcare Mater. 13 (2024) 202304060, https://doi.org/10.1002/adhm.202304060.

[12] Z. Wang, I.C.M. van der Geest, S.C.G. Leeuwenburgh, J.J.J.P. van den Beucken, Bifunctional bone substitute materials for bone defect treatment after bone tumor resection, Mater. Today Bio 23 (2023) 100889, https://doi.org/10.1016/j.mtbio.2023.100889.

[13] M.C. Tronco, J.B. Cassel, L.A. dos Santos, ?-TCP-based calcium phosphate cements: a critical review, Acta Biomater. 151 (2022) 70–87, https://doi.org/10.1016/j.actbio.2022.08.040.

[14] W. Dai, S. Li, H. Jia, X. Zhao, C. Liu, C. Zhou, Y. Xiao, L. Guo, Y. Fan, X. Zhang, Indirect 3D printing CDHA scaffolds with hierarchical porous structure to promote osteoinductivity and bone regeneration, J. Mater. Sci. Technol. 207 (2024) 295–307, https://doi.org/10.1016/j.jmst.2024.04.032.

[15] M. Janek, I. Vaskova, M. Pischova, R. Fialka, Z. Hajduchova, P. Veteska, J. Feranc, M.H. Orlovska, P. Peciar, E. Rakovsky, L. Baca, Characteristics of sintered calcium deficient hydroxyapatite scaffolds produced by 3D printing, J. Eur. Ceram. Soc. 44 (2024) 5284–5297, https://doi.org/10.1016/j.jeurceramsoc.2024.01.047.

[16] Y. Xia, X. Jing, X. Wu, P. Zhuang, X. Guo, H. Dai, 3D-printed dual-ion chronological release functional platform reconstructs neuro-vascularization network for critical-sized bone defect regeneration, Chem. Eng. J. 465 (2023) 143015, https://doi.org/10.1016/j.cej.2023.143015.

[17] D. Cheng, R. Ding, X. Jin, Y. Lu, W. Bao, Y. Zhao, S. Chen, C. Shen, Q. Yang, Y. Wang, Strontium ion-functionalized nano-hydroxyapatite/chitosan composite microspheres promote osteogenesis and angiogenesis for bone regeneration, ACS Appl. Mater. Interfaces 15 (2023) 19951–19965, https://doi.org/10.1021/acsami.3c00655.

[18] M. Wu, F. Chen, H. Liu, P. Wu, Z. Yang, Z. Zhang, J. Su, L. Cai, Y. Zhang, Bioinspired sandwich-like hybrid surface functionalized scaffold capable of regulating osteogenesis, angiogenesis, and osteoclastogenesis for robust bone regeneration, Mater. Today Bio 17 (2022) 100458, https://doi.org/10.1016/j.mtbio.2022.100458.

[19] X. Li, Q. Zhou, Y. Wu, C. Feng, X. Yang, L. Wang, Y. Xiao, K. Zhang, X. Zhu, L. Liu, Y. Song, X. Zhang, Enhanced bone regenerative properties of calcium phosphate ceramic granules in rabbit posterolateral spinal fusion through a reduction of grain size, Bioact. Mater. 11 (2022) 90–106, https://doi.org/10.1016/j.bioactmat.2021.10.006.

[20] U. Ripamonti, R. Duarte, Mechanistic insights into the spontaneous induction of bone formation, Biomater. Adv. 158 (2024) 213795, https://doi.org/10.1016/j.bioadv.2024.213795.

[21] L. Zhang, T. Lu, F. He, W. Zhang, X. Yuan, X. Wang, J. Ye, Physicochemical and cytological properties of poorly crystalline calcium-deficient hydroxyapatite with different Ca/P ratios, Ceram. Int. 48 (2022) 24765–24776, https://doi.org/10.1016/j.ceramint.2022.05.126.

[22] M.U. Farooq, C.H. Lawrie, N.-N. Deng, Engineering nanoparticles for cancer immunotherapy: current achievements, key considerations and future perspectives, Chem. Eng. J. 486 (2024) 150356, https://doi.org/10.1016/j.cej.2024.150356.

[23] Y. Lukina, T. Safronova, D. Smolentsev, O. Toshev, Calcium phosphate cements as carriers of functional substances for the treatment of bone tissue, Materials 16 (2023) 4017, https://doi.org/10.3390/ma16114017.

[24] X. Yuan, W. Zhu, Z. Yang, N. He, F. Chen, X. Han, K. Zhou, Recent advances in 3D printing of smart scaffolds for bone tissue engineering and regeneration, Adv. Mater. (2024) 202403641, https://doi.org/10.1002/adma.202403641.

[25] Y. Li, H. Qi, Y. Geng, L. Li, X. Cai, Research progress of organic photothermal agents delivery and synergistic therapy systems, Colloids Surf. B Biointerfaces 234 (2024) 113743, https://doi.org/10.1016/j.colsurfb.2024.113743.

[26] M. Overchuk, R.A. Weersink, B.C. Wilson, G. Zheng, Photodynamic and photothermal therapies: synergy opportunities for nanomedicine, ACS Nano 17 (2023) 7979–8003, https://doi.org/10.1021/acsnano.3c00891.

[27] Q. Wang, J. Chen, J. Ling, H. Zhao, X.-k. Ouyang, N. Wang, Metal-polyphenol network coated photothermal nanocarriers for pH-activated drug delivery, Mater. Today Chem. 35 (2024) 101892, https://doi.org/10.1016/j.mtchem.2023.101892.

[28] L. Che, Y. Wang, D. Sha, G. Li, Z. Wei, C. Liu, Y. Yuan, D. Song, A biomimetic and bioactive scaffold with intelligently pulsatile teriparatide delivery for local and systemic osteoporosis regeneration, Bioact. Mater. 19 (2023) 75–87, https://doi.org/10.1016/j.bioactmat.2022.03.023.

[29] S. Chen, D. Cheng, W. Bao, R. Ding, Z. Shen, W. Huang, Y. Lu, P. Zhang, Y. Sun, H. Chen, C. Shen, Y. Wang, Polydopamine-Functionalized strontium alginate/hydroxyapatite composite microhydrogel loaded with vascular endothelial growth factor promotes bone formation and angiogenesis, ACS Appl. Mater. Interfaces 16 (2024) 4462–4477, https://doi.org/10.1021/acsami.3c16822.

[30] L. Schirone, L. D'Ambrosio, M. Forte, R. Genovese, S. Schiavon, G. Spinosa, G. Iacovone, V. Valenti, G. Frati, S. Sciarretta, Mitochondria and doxorubicin-induced cardiomyopathy: a complex interplay, Cells 11 (2022) 2000, https://doi.org/10.3390/cells11132000.

[31] I.C. Jones, C.R. Dass, Doxorubicin-induced cardiotoxicity: causative factors and possible interventions, J. Pharm. Pharmacol. 74 (2022) 1677–1688, https://doi.org/10.1093/jpp/rgac063.

[32] J. Zhou, K. Li, H. Qin, B. Xie, H. Liao, X. Su, C. Li, X. He, W. Chen, X. Jiang, Programmed-stimuli responsive carrier-free multidrug delivery system for highly efficient trimodal combination therapy, J. Colloid Interface Sci. 637 (2023) 453–464, https://doi.org/10.1016/j.jcis.2023.01.091.

[33] C. Wang, Y. Zeng, K.-F. Chen, J. Lin, Q. Yuan, X. Jiang, G. Wu, F. Wang, Y.-G. Jia, W. Li, A self-monitoring microneedle patch for light-controlled synergistic treatment of melanoma, Bioact. Mater. 27 (2023) 58–71, https://doi.org/10.1016/j.bioactmat.2023.03.016.

[34] F. Liu, Z. Cheng, H. Yi, NIR light-activatable dissolving microneedle system for melanoma ablation enabled by a combination of ROS-responsive chemotherapy and phototherapy, J. Nanobiotechnol. 21 (2023) 61, https://doi.org/10.1186/s12951-023-01815-4.

[35] L. Wang, J. Bi, K. Sun, A. Li, Z. Yuan, F. Yang, J. Mao, Effect of inositol on the thermally induced crystallization and phase evolution of amorphous calcium phosphate, CrystEngComm 24 (2022) 7193–7199, https://doi.org/10.1039/d2ce01078j.

[36] L. Wang, J. Yang, J. Bi, K. Sun, A. Li, J. Mao, Competition and neutralization: thermally induced crystallization and phase evolution of amorphous calcium phosphate with cosubstitution of larger and smaller divalent cations, ACS Omega 8 (2023) 7602–7606, https://doi.org/10.1021/acsomega.2c07117.

[37] J. Chen, H. Zhou, Y. Fan, G. Gao, Y. Ying, J. Li, 3D printing for bone repair: coupling infection therapy and defect regeneration, Chem. Eng. J. 471 (2023) 144537, https://doi.org/10.1016/j.cej.2023.144537.

[38] G. Wang, Y. Miao, H. Gong, M. Sheng, J. Jing, M. Liu, J. Lu, Z. Gong, K. Ma, Direct ink writing of reaction bonded silicon carbide ceramics with high thermal conductivity, Ceram. Int. 49 (2023) 10014–10022, https://doi.org/10.1016/j.ceramint.2022.11.179.

[39] D.G. O'Shea, T. Hodgkinson, C.M. Curtin, F.J. O'Brien, An injectable and 3D printable pro-chondrogenic hyaluronic acid and collagen type II composite hydrogel for the repair of articular cartilage defects, Biofabrication 16 (2024) 015007, https://doi.org/10.1088/1758-5090/ad047a.

[40] H. Elsayed, A. Chmielarz, M. Potoczek, T. Fey, P. Colombo, Direct ink writing of three dimensional Ti_2AlC porous structures, Addit. Manuf. 28 (2019) 365–372, https://doi.org/10.1016/j.addma.2019.05.018.

[41] T. Sun, J. Han, S. Liu, X. Wang, Z.Y. Wang, Z. Xie, Tailor-made semiconducting polymers for second near-infrared photothermal therapy of orthotopic liver cancer, ACS Nano 13 (2019) 7345–7354, https://doi.org/10.1021/acsnano.9b03910.

[42] I.L. Bado, W. Zhang, J. Hu, Z. Xu, H. Wang, P. Sarkar, L. Li, Y.-W. Wan, J. Liu, W. Wu, H.C. Lo, I.S. Kim, S. Singh, M. Janghorban, A.M. Muscarella, A. Goldstein, P. Singh, H.-H. Jeong, C. Liu, R. Schiff, S. Huang, M.J. Ellis, M.W. Gaber, Z. Gugala, Z. Liu, X.H.F. Zhang, The bone microenvironment increases phenotypic plasticity of ER+ breast cancer cells, Dev. Cell 56 (2021) 1100, https://doi.org/10.1016/j.devcel.2021.03.008.

[43] C.-C. Ho, Y.-W. Chen, K. Wang, Y.-H. Lin, T.-C. Chen, M.-Y. Shie, Effect of mussel-inspired polydopamine on the reinforced properties of 3D printed β-tricalcium phosphate/polycaprolactone scaffolds for bone regeneration, J. Mater. Chem. B 11 (2022) 72–82, https://doi.org/10.1039/d2tb01995g.

[44] E. Bosch-Rue, L. Diez-Tercero, J.O. Buitrago, E. Castro, R.A. Perez, Angiogenic and immunomodulation role of ions for initial stages of bone tissue regeneration, Acta Biomater. 166 (2023) 14–41, https://doi.org/10.1016/j.actbio.2023.06.001.

[45] J. Nambiar, S. Jana, S.K. Nandi, Strategies for enhancing vascularization of biomaterial-based scaffold in bone regeneration, Chem. Rec. 22 (2022) e202200008, https://doi.org/10.1002/tcr.202200008.
[46] Y. Niu, L. Chen, T. Wu, Recent advances in bioengineering bone revascularization based on composite materials comprising hydroxyapatite, Int. J. Mol. Sci. 24 (2023) 12492, https://doi.org/10.3390/ijms241512492.
[47] H. Liu, H. Chen, Q. Han, B. Sun, Y. Liu, A. Zhang, D. Fan, P. Xia, J. Wang, Recent advancement in vascularized tissue-engineered bone based on materials design and modification, Mater. Today Bio 23 (2023) 100858, https://doi.org/10.1016/j.mtbio.2023.100858.